catalysts

MDPI

Article

Electrodeposition of a Li-Al Layered Double Hydroxide (LDH) on a Ball-like Aluminum Lathe Waste Strips in Structured Catalytic Applications: Preparation and Characterization of Ni-Based LDH Catalysts for Hydrogen Evolution

Song-Hui Huang [1], Yu-Jia Chen [1], Wen-Fu Huang [1] and Jun-Yen Uan [1,2,*]

[1] Department of Materials Science and Engineering, National Chung Hsing University, 145 Xingda Rd., Taichung 40227, Taiwan; d099066006@mail.nchu.edu.tw (S.-H.H.); t820207@gmail.com (Y.-J.C.); g106066012@mail.nchu.edu.tw (W.-F.H.)

[2] Innovation and Development Center of Sustainable Agriculture (IDCSA), National Chung Hsing University, 145 Xingda Rd., Taichung 40227, Taiwan

* Correspondence: jyuan@dragon.nchu.edu.tw; Tel.: +886-422-840-500-401

Abstract: A functionally structured catalyst was explored for ethanol steam reforming (ESR) to generate H_2. Aluminum lathe waste strips were employed as the structured catalytic framework. The mixed metal oxide (Li-Al-O) was formed on the surface of Al lathe waste strips through calcination of the Li-Al-CO_3 layered double hydroxide (LDH), working as the support for the formation of Ni catalyst nanoparticles. NaOH and $NaHCO_3$ titration solutions were, respectively, used for adjusting the pH of the $NiCl_2$ aqueous solutions at 50 °C when developing the precursors of the Ni-based catalysts forming in-situ on the Li-Al-O oxide support. The Ni precursor on the Al structured framework was reduced in a H_2 atmosphere at 500 °C for 3 h, changing the hydroxide precursor into Ni nanoparticles. The titration agent (NaOH or $NaHCO_3$) effectively affected the physical and chemical characterizations of the catalyst obtained by the different titrations. The ESR reaction catalyzed by the structured catalysts at a relatively low temperature of 500 °C was studied. The catalyst using $NaHCO_3$ titration presented good stability for generating H_2 during ESR, achieving a high rate of H_2 volume of about 122.9 L/(g_{cat}·h). It also had a relatively low acidity on the surface of the Li-Al-O oxide support, leading to low activity for the dehydration of ethanol and high activity to H_2 yield. The interactions of catalysts between the Ni precursors and the Li-Al-O oxide supports were discussed in the processes of the H_2 reduction and the ESR reaction. Mechanisms of carbon formation during the ESR were proposed by the catalysts using NaOH and $NaHCO_3$ titration agents.

Keywords: structured catalyst; ethanol steam reforming; aluminum lathe waste strips; layered double hydroxide; Ni nanoparticle

Citation: Huang, S.-H.; Chen, Y.-J.; Huang, W.-F.; Uan, J.-Y. Electrodeposition of a Li-Al Layered Double Hydroxide (LDH) on a Ball-like Aluminum Lathe Waste Strips in Structured Catalytic Applications: Preparation and Characterization of Ni-Based LDH Catalysts for Hydrogen Evolution. *Catalysts* **2022**, *12*, 520. https://doi.org/10.3390/catal12050520

Academic Editors: Ioan-Cezar Marcu and Octavian Dumitru Pavel

Received: 10 March 2022
Accepted: 2 May 2022
Published: 5 May 2022

1. Introduction

Renewable energy is sought to replace fossil fuels, which have caused environmental pollution, such as through the emission of greenhouse gases. Hydrogen is a clean and renewable energy carrier that can be used as a feedstock in fuel cell systems [1,2] and transportation [3]. Clean techniques for producing hydrogen are being developed, including the electrolysis of water [4], the photocatalysis of water [5,6], metal hydrolysis [7], the use of biomass [8], hydrocarbon reforming [2,9,10], and others. In recent decades, ethanol steam reforming (ESR) for hydrogen production has attracted interesting investigation due to its environmental benefits. Ethanol is a renewable raw material that can be produced in the fermentation of biomass, including sugar cane, corns, and in starch-rich and lignocellulosic materials [2,11,12]. The production of hydrogen by ESR is not only environmentally friendly but also highly efficient, unlike steam reforming for producing other fuels [13,14].

The overall steam reforming reaction of ethanol is given by Equation (1) [1,2,13–18].

$$C_2H_5OH + 3H_2O \rightarrow 6H_2 + 2CO_2 \ (\Delta H^0 = +173.5 \text{ kJ/mol}) \quad (1)$$

However, several side reactions may occur during the ESR process, depending on the species of catalyst used [2,13,19]. Catalysts play a crucial role in the ESR process. In addition to increasing the reaction rate, they activate ethanol conversion and hydrogen selection [2,13,18,19]. The use of noble metal catalysts (such as Rh, Ru, Pt, Pd, and Ir) and non-noble metal catalysts (such as Ni, Co, Cu, and Fe) in the ESR process has frequently been studied [2,13,16,18,19]. Noble metal catalysts have a high cost, limiting their widespread use in industry. A Ni-based catalyst has a lower cost and is effective in breaking C-C bonds and O-H bonds, as well as in CH_4 reforming [2,16,18–21]. Ni also favors the adsorption of hydrogen atoms on the catalyst surface to form molecular H_2 [2]. Accordingly, a Ni-based catalyst is used herein. Catalyst support selection is closely associated with the activity and stability of the catalyst [2,14,18]. Al_2O_3, working as catalyst support, is widely used for a Ni-based catalyst in the ESR process, owing to its good mechanical properties and thermal stability under reaction conditions [18,21,22]. However, at the acidic sites on Al_2O_3, ethanol can be dehydrated to ethylene, according to Equation (2) [2,13,14,16–21]:

$$C_2H_5OH \rightarrow C_2H_4 + H_2O \quad (2)$$

Finally, the polymerization of ethylene (C_2H_4) forms coke, causing the gradual deactivation of the catalyst. Furthermore, ethylene can be decomposed into carbon species, as described by Equation (3) [22]:

$$nC_2H_4 \rightarrow C_nH_{2n} + nH_2 \rightarrow nC + 2nH_2 \quad (3)$$

Some studies have found that basic additives or promoters, such as an alkali metal (such as Li, Na, and K) or an alkaline earth metal (such as Mg, Ca, and Sr) neutralize the acidic sites on Al_2O_3 [2,14,18]. Promoters favor H_2O adsorption and OH^- mobility on the Al_2O_3 surface, simultaneously accelerating carbon oxidation and reducing the rate of coke formation [21]. However, promoters do not disperse easily in the Al_2O_3 crystal structure or on the Al_2O_3 surface. Calcination of hydrotalcites i.e., layered double hydroxides (LDHs), at a high temperature can yield mixed metal oxides (MMO) [23–25]. The metal oxides are candidates for providing the support of catalyst particles in ESR. Favorable characteristics, such as a large surface area, thermal stability, and high metal dispersion, favor the use of LDHs in the ESR process [23,24,26–29]. LDHs are large classes of layered anionic clays. They have positively charged layers with divalent or trivalent metal cations at the octahedral sites of the hydroxyl slabs. Anions and water molecules intercalate the interlayer spaces with charge compensation [30–32]. Under special conditions, monovalent metal cations such as Li^+ occupy the vacancies in an aluminum octahedral sheet ($Al(OH)_3$) to form a positively charged layer [30–32]. For instance, Li-Al LDHs have the chemical formula $[LiAl_2(OH)_6]^+A^-{\cdot}mH_2O$, where A^- is an interlayered anion.

In this study, 500 °C-calcined Li-Al-CO_3 LDH is used as a support in the ESR process. Li-Al-CO_3 LDH after calcination at 500 °C may transform to Li-contained γ-Al_2O_3 [33,34]. Notably, Li^+ ions that are well dispersed in the γ-Al_2O_3 structure neutralize the acidic sites on the γ-Al_2O_3 surface. Hence, in this study, calcining LDHs at 500 °C to form Li-Al mixed metal oxides is expected to resolve some issues, such as the difficulty of dispersing promoters in oxide supports. In conventional fixed-bed reactors, the catalyst used for ESR is commonly in the form of powder or a powder-pressed pellet. A small-scale reactor not only has limited catalytic space, but also can be blocked by a large volume of carbon deposits during ESR [35,36]. Catalyst pellets, during ESR in a long-term reaction, may have coking problems, and the difficulties of thermal, chemical, and mechanical stresses, therefore, causing their disintegration and functional failure [35]. Developing stable catalysts with low carbon deposition when used in ESR is a challenge. Recently, structured catalysts

and reactors have attracted attention in the field of catalyst research owing to their rapid heat and mass transfer and lower pressure drop [36–40]. Classes of structured catalysts include monolithic catalysts, foam catalysts, membrane catalysts, and three-dimensional micro-fibrous entrapped catalysts (3D-MFEC) [36–40]. Among these, the framework of 3D-MFECs can be metallic or ceramic. A metal framework is better than a ceramic one because it has higher heat and mass transfer [39]. However, structured catalytic frameworks must be prepared precisely, and the process is complicated, resulting in a high cost. Therefore, a lower-cost and stable structured catalyst must urgently be developed. In this study, three-dimensional ball-like aluminum alloy lathe waste strips with a dense and disordered structure are used as a structured catalytic framework. Aluminum alloy lathe waste strips are not economically recycled in industry, because of the oxide, filth, and oil that adheres to their surfaces. Herein, the use of aluminum alloy lathe waste strips as a structured catalytic framework reduces not only the cost of the framework material but also the pollution of the environment by such wastes.

In this work, aqueous solutions that mainly contained Li^+ and Al^{3+} ions were used for the formation of Li-Al-CO_3 LDH thin film on Al lathe waste strips. An important discovery was that, following the electrochemical deposition, the LDH was calcined at 400 °C to increase the hydrophilicity, easily leading to the in-situ growth of Ni precursors on the calcined LDH platelets in $NiCl_2$ aqueous solutions at 50 °C by using NaOH or $NaHCO_3$ titration. The Ni precursors were activated in an H_2 atmosphere at 500 °C for 3 h. The structured catalysts prepared using NaOH and $NaHCO_3$ titration methods were tested in the ESR process at 500 °C. After the ESR reactions, H_2 yields and the interactions of nickel loading with calcined LDH support of the catalysts on product selectivity were analyzed. In addition, catalytic stabilities, acidic and basic properties on the surface of the catalysts, and the mechanisms of carbon deposition in prepared samples were discussed in detail.

2. Results and Discussion

2.1. Electrodeposition and Calcination of Li-Al-CO_3 LDH Thin Film/Characterization of Ni-Based Catalyst on Calcined LDH Support

Figure 1 plots the curve of current against electrolysis time during the deposition process. The initial current decayed rapidly, indicating the occurrence of the Li-Al-CO_3 LDH deposition on the surfaces of the Al lathe waste strips. Subsequently, the current approached a plateau at about 2000 to 7200 sec, implying that the non-conducted Li-Al-CO_3 LDH film had steadily grown as a function of time. The thin film that was formed using the electrochemical technique was examined using an X-ray diffractometer, as shown in Figure S1. Characteristic peaks of Li-Al-CO_3 LDH (hydrotalcite) (JCPDS card no. 42-729) and the Al substrate were observed. The X-ray diffraction (XRD) pattern suggests that the electrodeposition method successfully deposits the Li-Al-CO_3 LDH thin film on to the ball-like aluminum lathe waste strips. Wetting with water is an important procedure that can help the catalyst precursor to grow on the LDH platelets' surface. Figure S2 presents the water contact angle on the surfaces of the Al substrate, Li-Al LDH film @ Al substrate (denoted as L@Al), and the L@Al samples after calcination at 100–500 °C. The calcined Li-Al LDH film @ Al substrate had a lower water contact angle than the original Al substrate and Li-Al LDH film @ Al substrate. In particular, the 400 °C-calcined Li-Al LDH film @ Al substrate had the lowest water contact angle (the highest wettability with water). Therefore, calcination at 400 °C was performed before the preparation of Ni precursor on the LDH @ Al substrate. Figure 2a presents the SEM surface morphology of the electrodeposited Li-Al LDH thin film on the Al lathe substrate. Figure 2b zooms in on part of Figure 2a. The SEM images show a typical nanoplate's microstructure on the Al lathe substrate. Figure 2c shows the SEM image of the 400 °C-calcined Li-Al LDH thin film on Al lathe substrate. The SEM image demonstrates that calcination at 400 °C does not change the LDH surface microstructure.

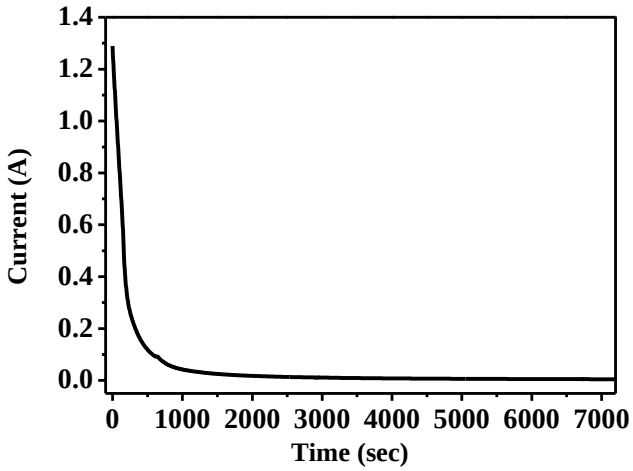

Figure 1. Current versus time curve during the electrochemical deposition of Li-Al-CO_3 LDH thin film in the Li^+/Al^{3+} aqueous solution at a constant potential. A DC voltage of 5 V was applied in the electrochemical cell for 2 h at room temperature.

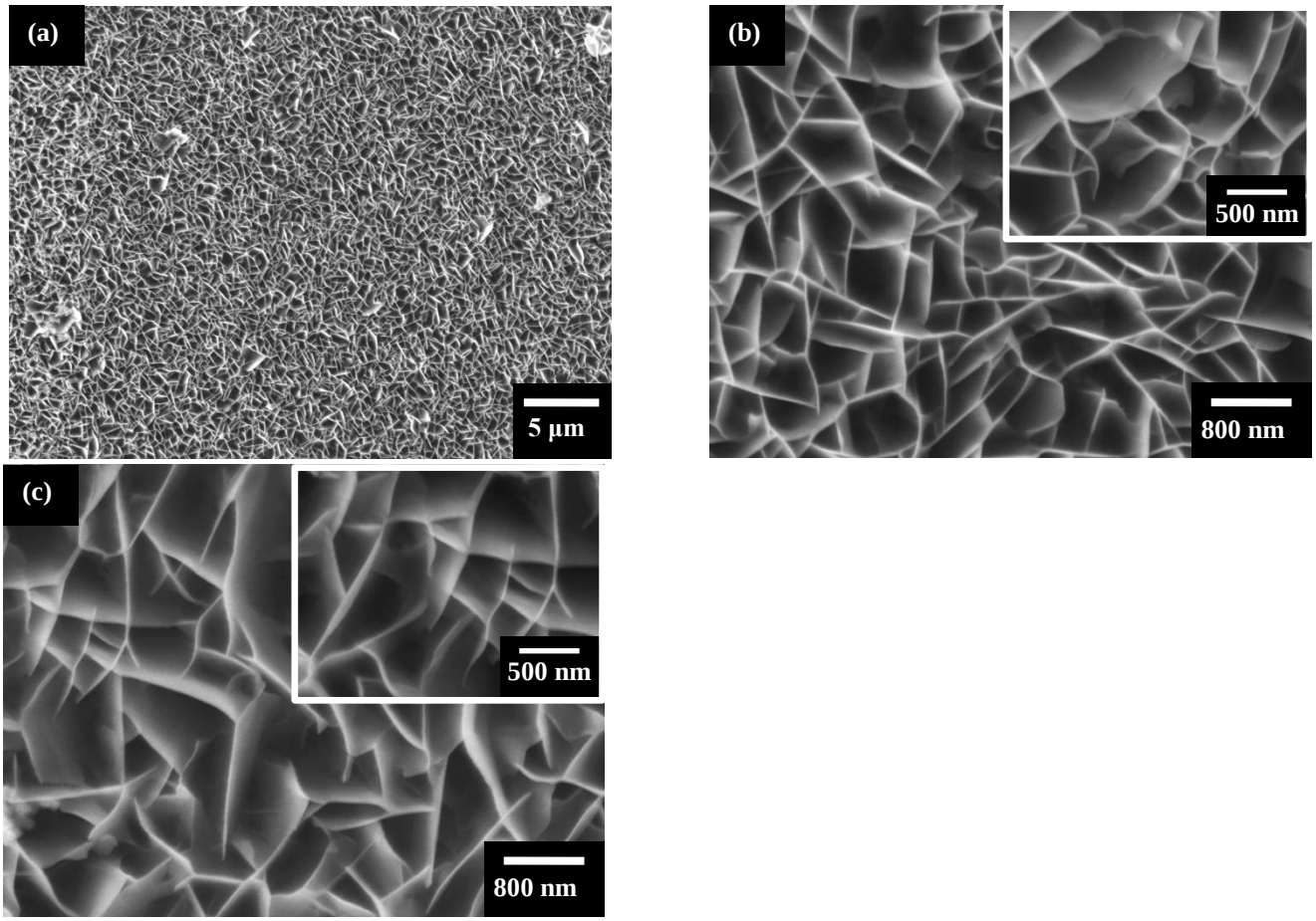

Figure 2. SEM surface morphologies: (**a**) Li-Al-CO_3 LDH thin film on Al substrate (A6061 lathe waste strip) and its high-magnification image in (**b**); (**c**) Li-Al-CO_3 LDH thin film calcined at 400 °C for 1 h.

Figure 3 shows the XRD patterns of Ni precursors (fresh catalysts) on the 400 °C-calcined LDH@Al substrates of the NaOH and $NaHCO_3$ prepared samples (denoted as NaOH_T and $NaHCO_3$_T). The two samples, NaOH and $NaHCO_3$, yield the same diffraction peaks at 2θ of 11°, 22.2°, 34.8°, 36.5°, 46°, 61.2°, which are characteristic of α-type nickel hydroxide (Ni catalyst precursor; $Ni(OH)_2 \cdot xH_2O$; JCPDS card no. 38-715). Sample

$NaHCO_3$_T yielded weak and broad peaks of $Ni(OH)_2$, while the sample NaOH_T yielded intensive peaks of $Ni(OH)_2$. The results suggest that the $Ni(OH)_2$ (Ni catalyst precursor) for sample $NaHCO_3$_T probably had poor crystallinity with nano-size structure, while the $Ni(OH)_2$ on NaOH_T had good crystallinity. The patterns of both samples also include diffraction peaks of the Al substrate. However, the calcined LDH phase was not observed in the patterns of either sample. In our previous study [25], calcining LDH at 300–400 °C formed an amorphous-like mixed metal oxide (MMO). Accordingly, intensive diffraction peaks of the calcined LDH phase were not present in the patterns of the NaOH_T and $NaHCO_3$_T samples, owing to their amorphous-like structure.

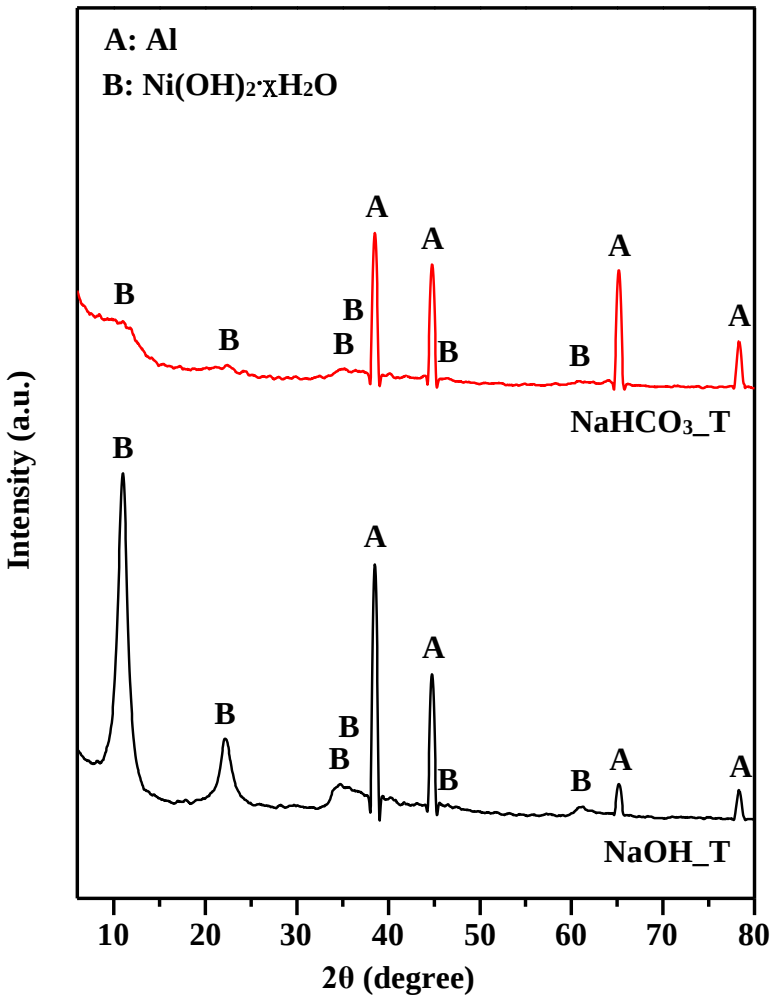

Figure 3. XRD patterns of Ni precursors (fresh catalysts) on the 400 °C calcined LDH@Al substrates for the sample NaOH_T (bottom pattern) and $NaHCO_3$_T (top pattern), respectively.

As shown in Figure 4a,b for the SEM microstructures of NaOH_T (fresh catalyst) and NaOH_T + R (reduced catalyst), Figure 4a displays the SEM surface observation on NaOH_T. Figure 4b shows the SEM surface microstructure of the NaOH_T + R. A few nanoparticles are presented in the calcined LDH platelets. As shown in Figure 4c,d, Figure 4c displays the SEM surface microstructure of the $NaHCO_3$_T, showing the cross-linked meshwork structures on platelets. Figure 4d presents the SEM surface microstructure of the sample $NaHCO_3$_T + R after H_2 reduction. Many nanoparticles are dispersed uniformly on the edges and platelets of the calcined LDH.

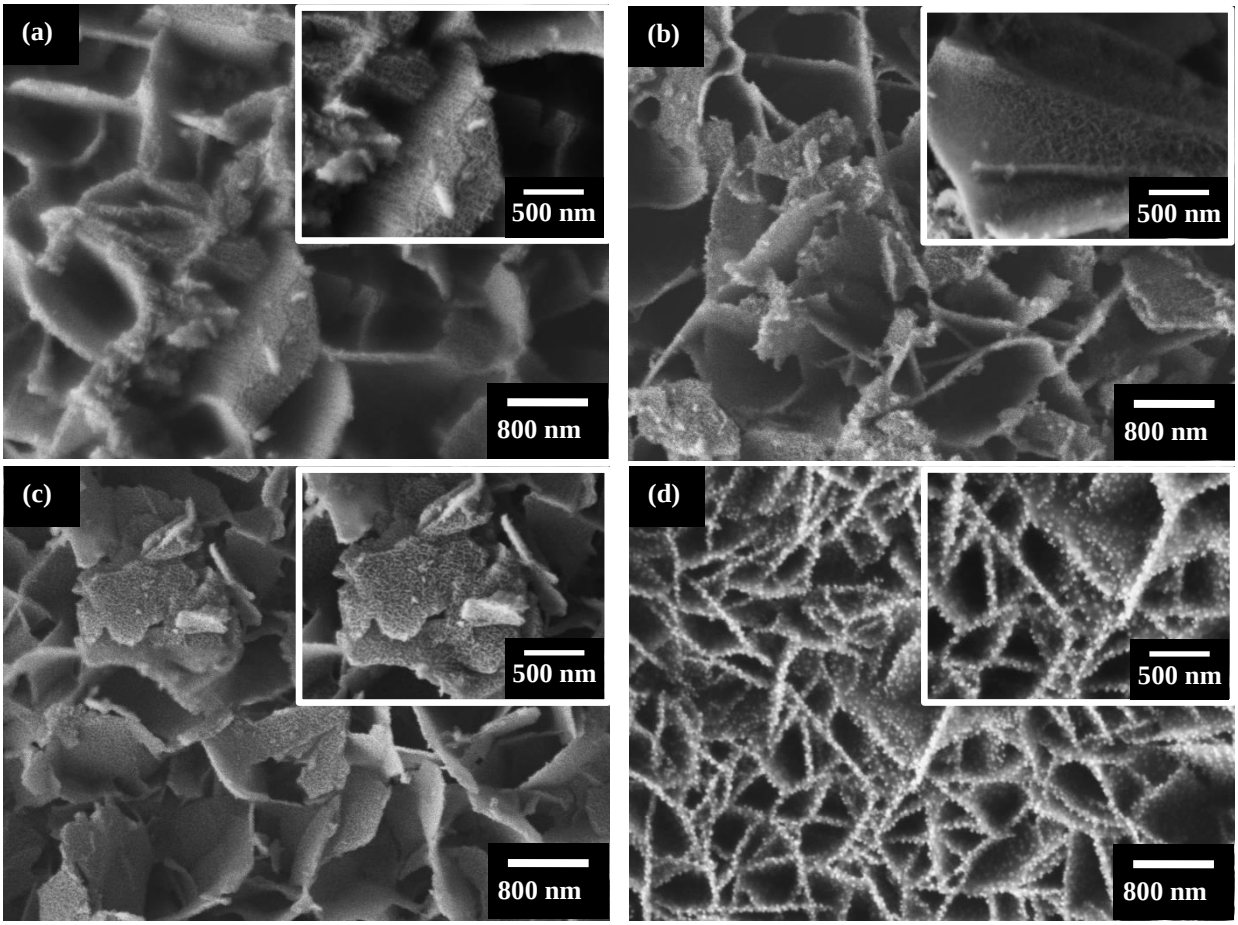

Figure 4. SEM surface morphologies: (**a**) NaOH_T fresh catalyst; (**b**) NaOH_T + R reduced catalyst; (**c**) $NaHCO_3$_T fresh catalyst; (**d**) $NaHCO_3$_T + R reduced catalyst.

2.2. Use of the Structured Catalyst in Ethanol Steam Reforming (ESR) Reaction

Figure 5a plots the H_2 yields as a function of time during ESR reactions. The H_2 yield (Y_{H2}) can be expressed below:

$$Y_{H_2} = \text{mole of } H_2 \text{ output/mole of ethanol input} \quad (4)$$

The ESR reaction catalyzed by the NaOH_T + R or by the $NaHCO_3$_T + R catalyst produced different H_2 yields. The $NaHCO_3$_T + R catalyst gave a stable H_2 yield of about 55%, higher than that obtained using the NaOH_T + R catalyst. The H_2 yield of NaOH_T + R catalyst decreased with time and rapidly dropped after 4.3 h. Figure 5b plots the cumulative volume of H_2 produced per gram of the catalyst by using the NaOH_T + R or $NaHCO_3$_T + R catalyst during the ESR reaction for 5 h. The cumulative volume of H_2 produced by the $NaHCO_3$_T + R catalyst increased linearly with time from the beginning to the end of the ESR reaction, indicating a constant rate of H_2 generation. The cumulative volume of H_2 was 614.5 L/g_{cat} after 5 h of ESR. Restated, the cumulative volume of H_2 per hour was about 122.9 $L/(g_{cat} \cdot h)$. The cumulative volume of H_2 that was obtained using NaOH_T + R catalyst was around 435.9 L/g_{cat}, less than that produced by the $NaHCO_3$_T + R catalyst. The cumulative volume of H_2 per hour was about 87.2 $L/(g_{cat} \cdot h)$. Figure 5c,d present the compositions of the gases that were produced using the NaOH_T + R and $NaHCO_3$_T + R catalysts in ESR reactions for 5 h. The main gaseous productions were H_2, CO_2, CO, and CH_4. As shown in Figure 5c, the H_2 produced (Vol.%) by the NaOH_T + R catalyst generally fell with time, and rapidly dropped after 4.3 h. This result is consistent with the H_2 yield in Figure 5a. As shown in Figure 5d, the gas productions (H_2, CO_2, CO, and CH_4) had a stable output from the beginning to the end of the ESR reaction.

Importantly, the gas production remained about 70 Vol.% of H_2 until the reaction stopped. Frusteri et al., [41] reported that a doping with Li increased the stability of the Ni/MgO catalyst for ESR, mainly by reducing the sintering of the Ni catalyst particles. Herein, the $NaHCO_3$_T + R catalyst with the LiAlO mixed metal support powerfully and stably activated ESR for H_2 generation. However, with the NaOH_T + R catalyst, H_2 production rapidly declined after 4.3 h; the possible reason will be discussed in the following section.

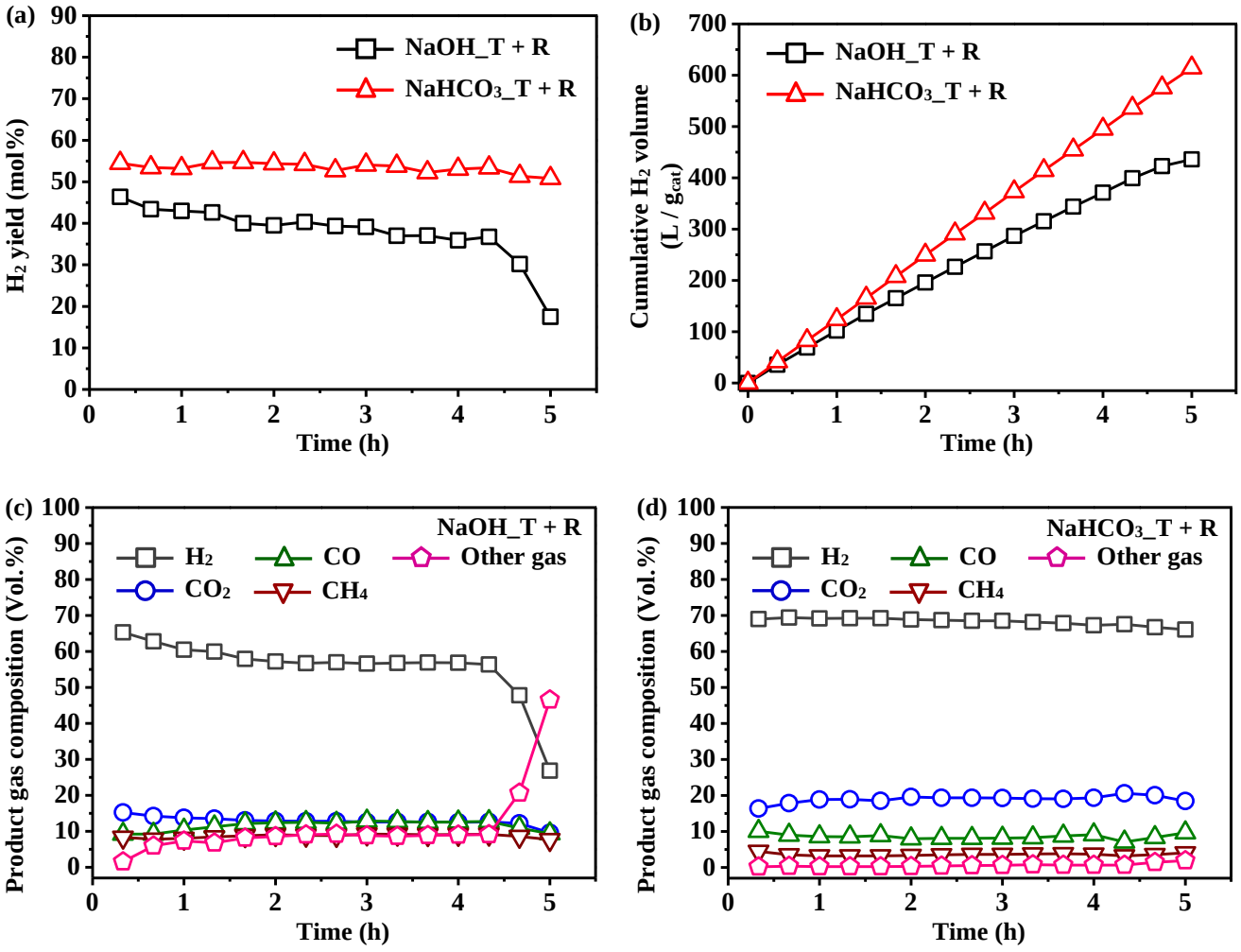

Figure 5. (**a**) H_2 yields and (**b**) cumulative H_2 volumes of the NaOH_T + R and $NaHCO_3$_T + R catalysts in the ESR reactions; Volume percentages of product gas composition of the NaOH_T + R catalyst (**c**) and $NaHCO_3$_T + R catalyst (**d**) in the ESR reactions.

The ethanol conversions (X_{EtOH}) and selectivity (S) of the productions after ESR reactions catalyzed by the NaOH_T + R and $NaHCO_3$_T + R catalysts were calculated using Equations (5)–(7) and were provided in Table 1.

$$X_{EtOH}\ (\%) = \frac{F_{\text{ethanol, in}} - F_{\text{ethanol,out}}}{F_{\text{ethanol,in}}} \quad (5)$$

$$S_{H_2}\ (\%) = \frac{F_{H_2\ \text{produced}}}{3 \times (F_{\text{ethanol,in}} - F_{\text{ethanol,out}}) + (F_{\text{water,in}} - F_{\text{water,out}})} \times 100 \quad (6)$$

$$S_{i\ \text{carbon-containing product}}\ (\%) = \frac{F_{i\ \text{carbon-containing product}}}{n_i \times (F_{\text{ethanol,in}} - F_{\text{ethanol, out}})} \times 100 \quad (7)$$

where $F_{i,\,in/out}$ is the molar flow rate of the i specie at the inlet/outlet of the reactor, respectively, and n_i is the stoichiometric factor between the carbon-containing products and ethanol.

Table 1. Activations of the NaOH_T + R and $NaHCO_3$_T + R catalysts in the ESR reactions for 5 h: the averages of the ethanol conversion, selectivity of the production, and deposition weight of carbon species.

Catalyst	Conversion (%), Selectivity (mol%) and Deposition of Carbon Species ($g/(g_{cat}\cdot h)$)									
	X_{EtOH}	H_2	CO_2	CO	CH_4	C_2H_4	$(C_2H_5)_2O$	CH_3CHO	CH_3COCH_3	C
NaOH_T + R	30.35	37.97	13.27	11.59	8.82	20.93	7.40	40.58	1.14	0.943
$NaHCO_3$_T + R	21.94	74.04	30.84	13.91	5.80	11.01	2.57	43.21	0.77	0.869

In the analyses of the selectivity of the production, the chemical reaction pathways associated with ESR can be presumed be reducible to the following individual reactions [1,2,13–18].

$$C_2H_5OH + H_2O \rightarrow CH_4 + CO_2 + 2H_2 \quad (8)$$

$$C_2H_5OH \rightarrow CH_4 + CO + H_2 \quad (9)$$

$$2C_2H_5OH \rightarrow CH_3COCH_3 + CO + 3H_2 \quad (10)$$

$$2C_2H_5OH \rightarrow (C_2H_5)_2O + H_2O \quad (11)$$

$$C_2H_5OH \rightarrow CH_3CHO + H_2 \quad (12)$$

$$CH_3CHO \rightarrow CH_4 + CO \quad (13)$$

$$CH_3CHO + H_2O \rightarrow 2CO + 3H_2 \quad (14)$$

$$CH_4 + H_2O \rightarrow CO + 3H_2 \quad (15)$$

$$CO + H_2O \rightarrow CO_2 + H_2 \quad (16)$$

Table 1 shows the ethanol conversions after ESR reactions, and that the NaOH_T + R catalyst had a higher conversion (~30.35%) than the $NaHCO_3$_T + R catalyst (~21.94%). However, the H_2 selectivity (~37.97 mol%) by the NaOH_T + R catalyst was lower than that of the H_2 selectivity (~74.04 mol%) of the reaction catalyzed by $NaHCO_3$_T + R. Owing to the low H_2 selectivity, the application of the NaOH_T + R catalyst resulted in relatively low values of the selectivity of CO_2, CO, and CH_4, as shown in Table 1; they are 13.27 mol% of CO_2, 11.59 mol% of CO, and 8.82 mol% of CH_4, respectively. For comparison, the CO_2 selectivity was high up to 30.84 mol% when the $NaHCO_3$_T + R was employed, and this value was much higher than that of the CO_2 selectivity of 13.27 mol% catalyzed by the NaOH_T + R. Fundamentally, the high selectivity to CO_2 mainly represents that the ethanol steam reforming, as shown in Equation (8), and the water gas shift reaction, as shown in Equation (16) must proceed to produce CO_2. That is, the ethanol steam reforming of Equation (8), and water gas shift reaction of Equation (16) were not so well catalyzed while using the sample NaOH_T + R as the catalyst. In addition, the fact that CO_2 production exceeds CO production, especially when using the $NaHCO_3$_T + R catalyst (see Table 1), suggests a strong water gas shift reaction, as shown in Equation (16). Moreover, the high acetaldehyde selectivity (~40% up) of the two samples were detected in the ESR residual solutions. It implies that the reduced catalysts in both samples had successfully activated the ethanol dehydrogenation to acetaldehyde, as seen in Equation (12). Moreover, CH_4 can be easily produced in the ESR reaction process, as seen in Equations (8), (9) and (13). The methane steam reforming, as in Equation (15), was one of the main subreactions during ESR to consume CH_4 and produce H_2 (with one mole of CH_4 producing three moles of H_2). As shown in Table 1, the selectivity to CH_4 by the NaOH_T + R catalyst was 8.82 mol%, while the selectivity to CH_4 by the $NaHCO_3$_T + R catalyst was

only 5.80 mol%. Therefore, it suggests that the $NaHCO_3$_T + R catalyst promoted the methane steam reforming, as seen in Equation (15), to consume more CH_4 and to produce a larger amount of H_2 than those in the case of the NaOH_T + R catalyst. Furthermore, the ethanol dehydrated to produce the non-desirable C_2H_4, as seen in Equation (2), and $(C_2H_5)_2O$, as seen in Equation (11) was also detected in Table 1. The high C_2H_4 selectivity (~20.93 mol%) and $(C_2H_5)_2O$ selectivity (~7.40 mol%) were produced by the NaOH_T + R catalyst. When compared to the NaOH_T + R catalyst, the $NaHCO_3$_T + R catalyst had less C_2H_4 selectivity (~11.01 mol%) and $(C_2H_5)_2O$ selectivity (~2.57 mol%). The polymerization of ethylene caused the deposition of carbon species on the catalyst's surface, as described by Equation (3). Correspondingly, the NaOH_T + R catalyst had the higher carbon formation of 0.943 g/(g_{cat}·h) than that catalyzed by the $NaHCO_3$_T + R catalyst (~0.869 g/(g_{cat}·h)). In summary of the above description, the $NaHCO_3$_T + R catalyst, due to the relatively high selectivity to H_2, the high selectivity of CO_2, and the low selectivity of CH_4, C_2H_4, and $(C_2H_5)_2O$, it is explained that the $NaHCO_3$_T + R catalyst exhibited better catalysis performance in the ESR reaction than the NaOH_T + R catalyst.

2.3. Ni-Based Catalysts on Calcined LDH Supports: Comparison between NaOH and $NaHCO_3$ Titration in Preparation of the Catalysts

Figure 6 presents the FT-IR spectra of the samples NaOH_T and $NaHCO_3$_T. The intense broadband at around 3425 cm^{-1} is consistent with the stretching vibration of hydroxyl groups that are hydrogen-boned to H_2O [42–47]. A band near 1632 cm^{-1} is attributed to the H_2O bending vibration [42,44–47]. The tiny absorption band at 2403 cm^{-1} is attributed to the CO_2 adsorbed on the sample surface, because the prepared samples were grown in the atmosphere [44,45]. Another tiny band, at about 2125 cm^{-1}, reflected the presence of intercalated C–O species in the precursors [47]. The narrow band at 1376 cm^{-1} is assigned to the asymmetric stretching vibration of CO_3^{2-} [42,44,46,47]. A band around 847 cm^{-1} corresponded to an asymmetric stretching vibration of intercalated C–O species [44,46]. Two bands at about 612 cm^{-1} and 550 cm^{-1} are attributed to the in-plane deformations δ_{OH}, which are associated with the stretching vibration of Ni-OH [42,43,45,47]. Importantly, the FT-IR spectra revealed the vibrational bands of the OH group (~3425 cm^{-1}) and the Ni-OH group (~612 cm^{-1}), confirmed that the precursors of both samples were α-$Ni(OH)_2$ [43].

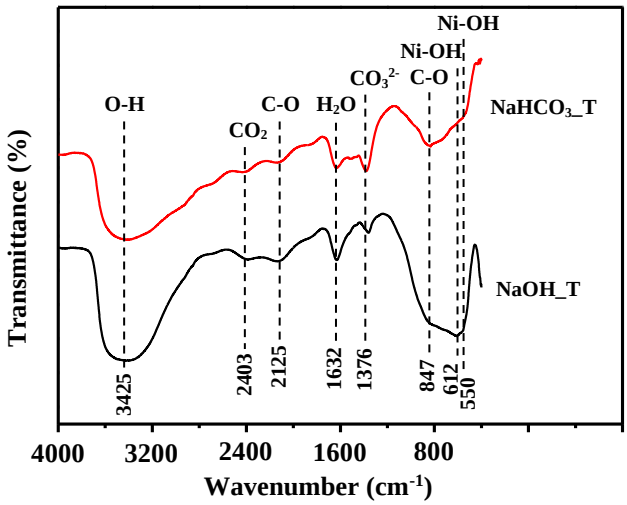

Figure 6. FT-IR spectra of Ni precursors (fresh catalysts) on the 400 °C-calcined LDH platelets of the samples NaOH_T and $NaHCO_3$_T.

Figure 7a,b present the SEM images and EDS compositional mappings of the samples NaOH_T and $NaHCO_3$_T. Ni and O were dispersed uniformly in the maps, indicating that the deposited $Ni(OH)_2$ were dispersed on the calcined LDH support. Figure 7c displays

statistics concerning the Ni, Al, and O element contents of the samples NaOH_T and $NaHCO_3$_T. The average Ni content in NaOH_T was more than double that in $NaHCO_3$_T. The high Ni content in NaOH_T is also clearly evident in the FT-IR spectra (Figure 6), which exhibits a higher O-H vibration band (~3425 cm^{-1}), H_2O vibration band (1632 cm^{-1}), and Ni-OH vibration bands (612 and 550 cm^{-1}), than those of the sample $NaHCO_3$_T.

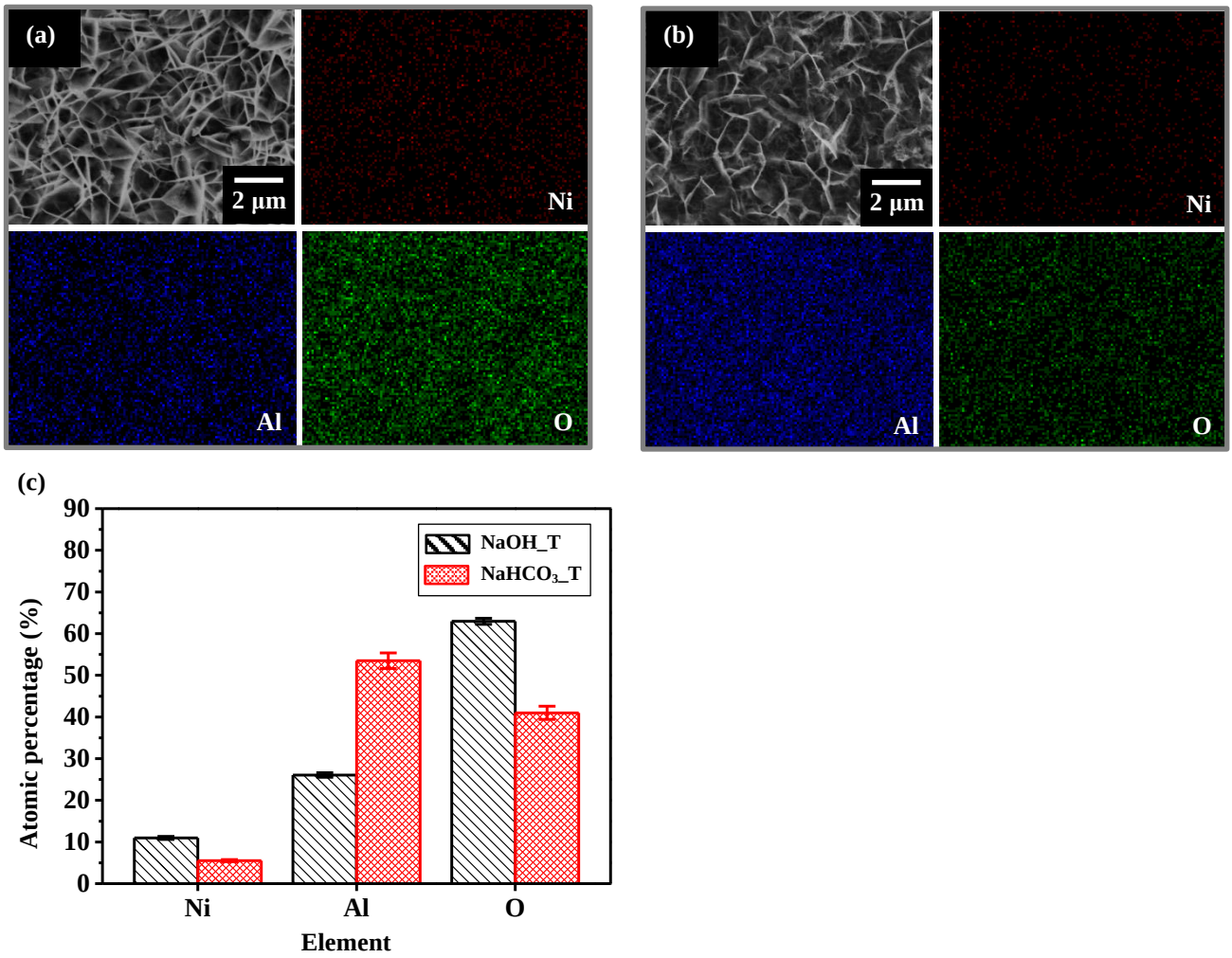

Figure 7. SEM surface morphologies of the sample NaOH_T and $NaHCO_3$_T with compositional maps for Ni, Al, and O are shown in (**a**,**b**), respectively; (**c**) EDS analyses of the elemental compositions and contents of the samples NaOH_T and $NaHCO_3$_T.

The above results suggest that sample NaOH_T had twice as much $Ni(OH)_2 \cdot xH_2O$ on the calcined LDH support as sample $NaHCO_3$_T. Calcining $Ni(OH)_2 \cdot xH_2O$ at 500 °C decomposed it to yield NiO [48,49]. The thermal decomposition reaction is as follows [48,49].

$$Ni(OH)_2 \cdot xH_2O_{(s)} \rightarrow Ni(OH)_{2(s)} + xH_2O_{(g)} \quad (17)$$

$$Ni(OH)_{2(s)} \rightarrow NiO_{(s)} + H_2O_{(g)} \quad (18)$$

where x is the amount of water in moles.

Equation (17) is the dehydration reaction of $Ni(OH)_2 \cdot xH_2O$, and Equation (18) is the decomposition of $Ni(OH)_2$ to NiO. Therefore, in this study, four times as much water vapor was produced from the nickel precursor of sample NaOH_T in the reduction process with an H_2 atmosphere at 500 °C than was produced from the nickel precursor of sample $NaHCO_3$_T. However, previous studies have reported [50–52] that a reduction reaction experiment for $NiO@Al_2O_3$ powder was carried out under an atmosphere with H_2 and

water vapor, resulting in decreased amounts of the reduced Ni metallic particles. This is because, at high temperature, Al_2O_3 in the water vapor atmosphere easily forms aluminate, leading to the reduced nickel reacting with vicinal aluminate to form surface nickel aluminate ($NiAl_2O_4$) [50–52]. Zieliński claimed [52] that $NiAl_2O_4$ content depended on the concentration of water vapor in the environment. In particular, when $NiO@Al_2O_3$ powder was heated at 450 °C in a water vapor atmosphere in an H_2 reduction process, nickel aluminate was produced quickly. Nonstoichiometric $NiAl_2O_4$ that decorates the corners and edges of nickel crystallites retards NiO reduction and weakens catalyst performance. Previous studies [33,34] found that calcining Li-Al LDH at 500 °C transforms the crystal mainly into γ-Al_2O_3. In this study, the precursor ($Ni(OH)_2 \cdot xH_2O$) on a calcined LDH (γ-Al_2O_3) support of the sample NaOH_T may possess an excessive concentration of water vapor (in comparison to $NaHCO_3$_T) in the H_2 reduction process, inhibiting the reduction of $Ni(OH)_2 \cdot xH_2O$ to Ni particles. Hence, as shown in the SEM image of NaOH_T + R in Figure 4b, fewer Ni particles were found on the calcined LDH platelets than were found as shown in $NaHCO_3$_T + R (Figure 4d). Figure 8 presents a TEM dark-field image of sample NaOH_T + R, and the inset presents the TEM diffraction pattern from the dark-field image in Figure 8. The diffraction pattern exhibits the characteristic Bragg reflections of NiO and Ni, suggesting that NiO and Ni crystallites were presented together on the NaOH_T + R catalyst. The $NiAl_2O_4$ may not demonstrate much infraction, leading to no evident diffraction pattern.

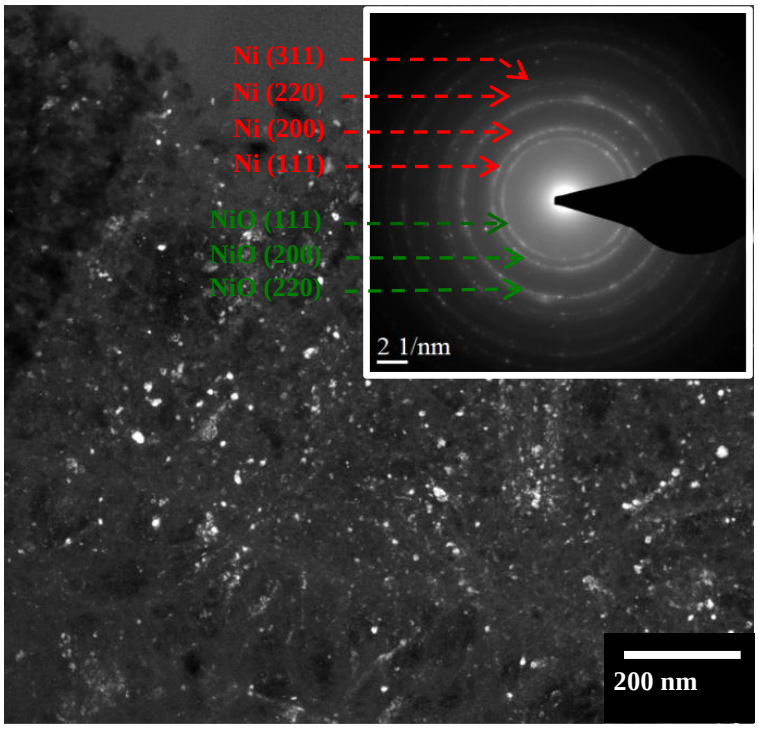

Figure 8. Dark-field image of the TEM cross-sectional microstructure of the NaOH_T + R catalyst. The inset shows the diffraction pattern of the bright particles from the TEM image.

Figure 9 exhibits the Ni $2p_{3/2}$ XPS spectra of the reduced NaOH_T + R and $NaHCO_3$_T + R catalysts. The binding energy of metallic Ni (Ni^0) is around 852.5 eV, and the accompanying shake-up satellite peak is observed at about 861.5 eV [21,53,54]. A peak at around 855.3 eV, which is characteristic of Ni^{2+}, is associated with NiO [53,54]. The NiO (Ni^{2+}) peaks from both reduced catalysts were higher than that of metallic Ni (Ni^0), perhaps because of the high oxygen affinity of nano-scale Ni particles [55]. Table 2 presents the surface compositions and quantitative elemental analyses of the reduced NaOH_T + R and $NaHCO_3$_T + R catalysts, as determined by XPS. The $NaHCO_3$_T + R catalyst had twice the Ni content (17.54 at.%) than that of NaOH_T + R catalyst (7.83 at.%). These results are consistent with

the SEM images previously shown in Figure 4, and reveal that a relatively high amount of the reduced Ni particles were dispersed on $NaHCO_3$_T + R.

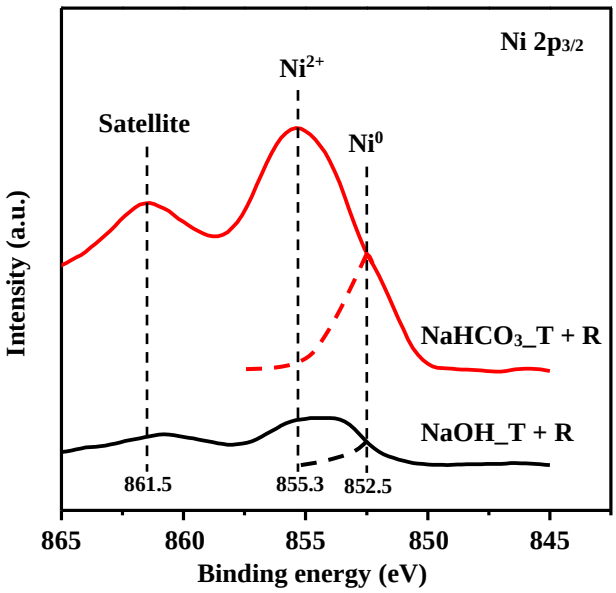

Figure 9. Ni $2p_{3/2}$ XPS spectra of the reduced NaOH_T + R and $NaHCO_3$_T + R catalysts.

Table 2. The quantitative elements and surface compositions of the reduced NaOH_T + R and $NaHCO_3$_T + R catalysts on the 500 °C calcined LDH thin films by XPS analysis.

Element	NaOH_T + R (at.%)	$NaHCO_3$_T + R (at.%)
Ni	7.83	17.54
Al	10.16	13.73
O	82.01	68.74

Figure 10a presents the TEM cross-sectional microstructure of the $NaHCO_3$_T + R catalyst; the image shows that Ni particles were dispersed uniformly on the platelet of the 500 °C-calcined LDH. Figure 10b shows the size distributions of the Ni particles on sample $NaHCO_3$_T + R, as obtained from the TEM image. The mean particle size is 10.7 nm. For comparison, Figure 10c shows the size distributions of the Ni particles that were measured using the TEM image on sample NaOH_T + R. The mean particle size is 14.6 nm. Figure S3 displays the TEM images of the Ni particles of sample NaOH_T + R and $NaHCO_3$_T + R. The above results suggest that the reduced Ni particles in sample $NaHCO_3$_T + R were more dispersed, smaller, and more numerable than in sample NaOH_T + R. The result may explain that the $NaHCO_3$_T + R catalyst for the ESR reaction resulted in a higher H_2 yield than the ESR results for the reaction catalyzed by the NaOH_T + R catalyst (Figure 5).

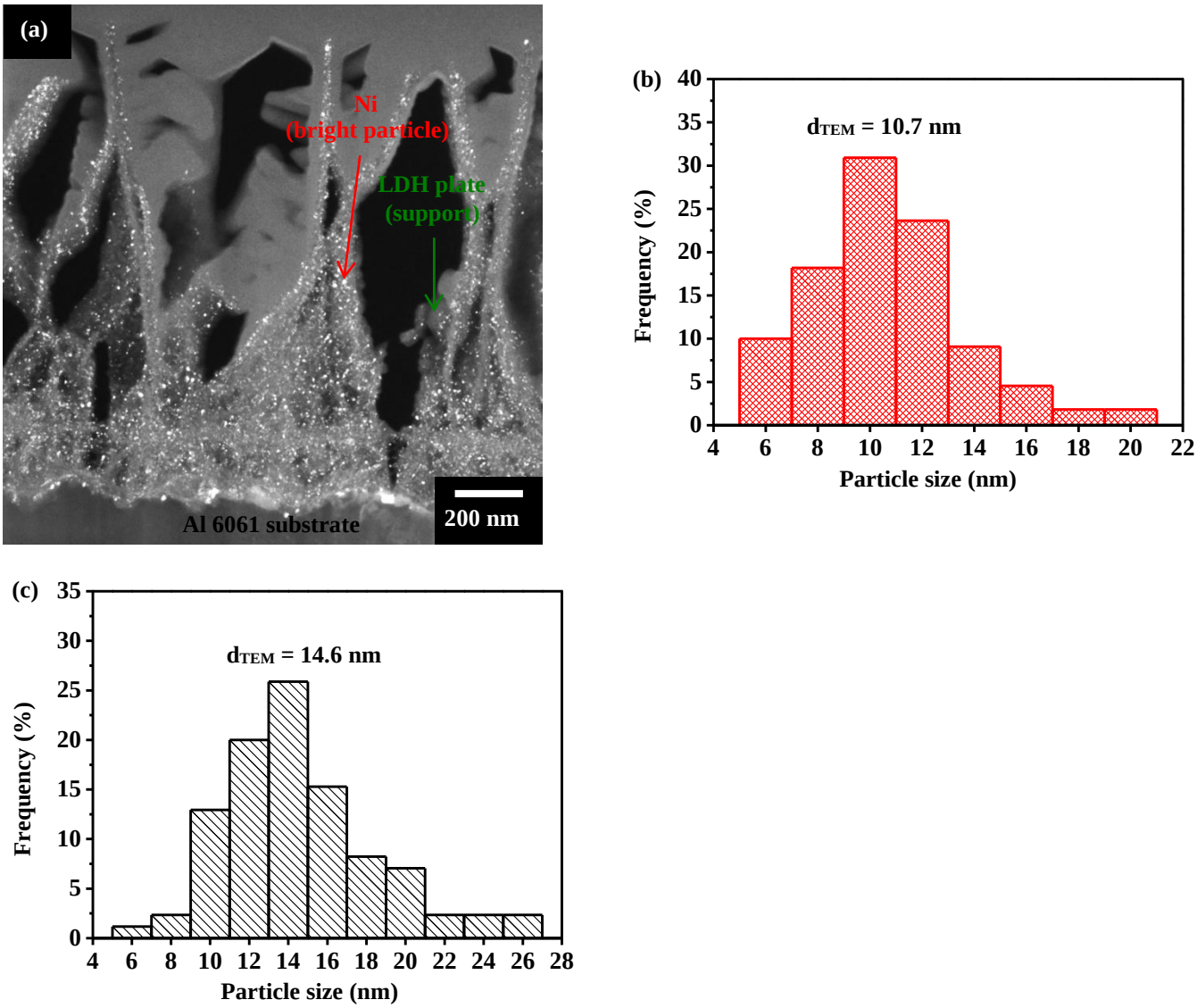

Figure 10. (**a**) TEM cross-sectional microstructure of the $NaHCO_3$_T + R catalyst; Particle size distributions of the $NaHCO_3$_T + R catalyst (**b**) and NaOH_T + R catalyst (**c**). The particle size distributions in (**b**,**c**) were collected from the TEM images in Figure S3.

2.4. Mechanism of Carbon (Coke) Formation in Ethanol Steam Reforming (ESR) Reaction

Figure 11 shows the SEM surface morphologies of the NaOH_T + R catalyst (Figure 11a) and $NaHCO_3$_T + R catalyst (Figure 11b), respectively, after ESR for 5 h. As shown, carbon filaments (filamentous cokes) were observed in both catalysts after the ESR reaction. The inset SEM micrographs in high magnification are also presented in Figure 11a,b, clearly indicating the carbon filaments and the Ni particles that were lifted at the top of the filaments. The size of the filaments on sample NaOH_T + R (Figure 11a) is much larger than that of the filaments on sample $NaHCO_3$_T + R (Figure 11b), As mentioned in Section 3.3, a higher Ni content on the $NaHCO_3$_T + R catalyst revealed a higher catalytic activity than in the NaOH_T + R catalyst. It is reasonable to interpret that fine carbon fiber filaments formed on the $NaHCO_3$_T + R catalyst (Figure 11b) due to the slower carbon growth rate. Inversely, the coarse carbon filaments formed on the NaOH_T + R catalyst due to a relatively high carbon growth rate. Figure 11c, taking the sample $NaHCO_3$_T + R as an example, displays the EDS spectrum for analyzing the surface elemental compositions of the bright particle on the top of the woven carbon filament after the ESR for 5 h. As shown,

a high-intensity peak of Ni was found. The result proves that the Ni particles were lifted from the supports of calcined LDH at the tops of the carbon filaments.

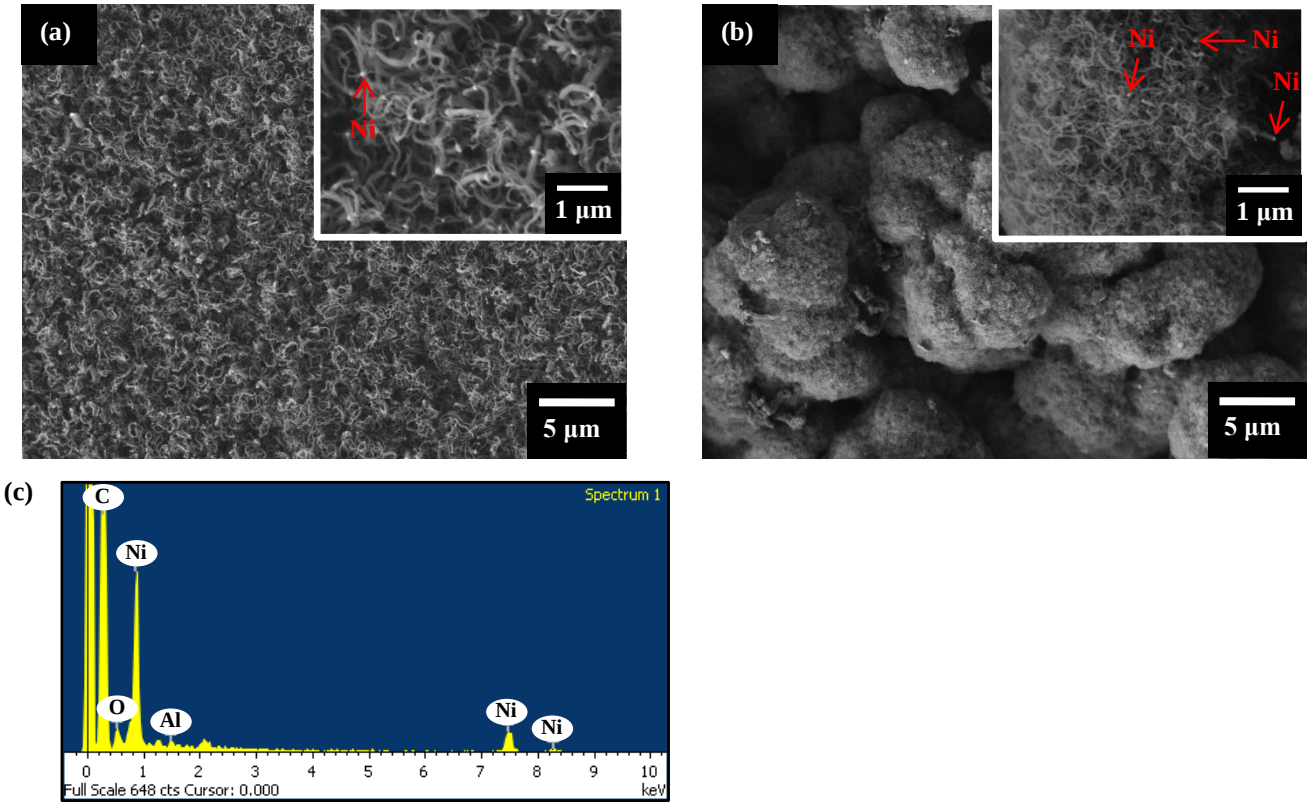

Figure 11. SEM surface morphologies of the catalysts after ESR reactions for 5 h: (**a**) NaOH_T + R catalyst; (**b**) $NaHCO_3$_T + R catalyst; (**c**) EDS spectrum presented as the high Ni contents were detected at bright particles on the tips of filamentous carbons in the SEM images (**a**,**b**).

An active catalyst can also exhibit the condition of carbon deposition and carbon interaction with supports after the catalyst has worked. The mechanisms of carbon deposition on the surfaces of catalysts (NaOH_T + R and $NaHCO_3$_T + R) and carbons interaction with Ni and calcined LDH supports during the ESR reactions are illustrated in Figure 12. The schematic models in Figure 12 (I)–(III) show this in atomic-scales, and Figure 12 (IV) shows this in nano-scale. Figure 12a (I) and 12b (I) are the schematic models of the crystal of the fresh catalysts (Ni precursors, NiO_xH_z) obtained, respectively, using the NaOH titration solution, as in Figure 12a (I), and the $NaHCO_3$ titration solution, as in Figure 12b (I). As schematically shown, the fresh catalysts (NaOH_T and $NaHCO_3$_T) were grown on the calcined LDH platelets. The precursor by NaOH titration, as in Figure 12a (I), has a much larger size than the precursor by $NaHCO_3$ titration, as in Figure 12b (I). In Figure 3 in Section 2.1, X-ray diffraction results of the precursor of sample $NaHCO_3$_T exhibited a much broader FWHM (full width at half maximum) (1.64°) than the FWHM (0.51°) of the strong peaks of the $Ni(OH)_2$ by sample NaOH_T, suggesting that the titration of the $NaHCO_3$ solution produced a much finer crystallite size of $Ni(OH)_2$ precursor than those produced by NaOH titration, according to the fundamental concept of the Scherrer equation to estimate nano-crystallite size. More $Ni(OH)_2$ precursors on the calcined LDH support in the NaOH_T catalyst suggest that the abundant water vapor would cause NiO_xH_z interaction with calcined LDH (γ-Al_2O_3) supports to form $NiAl_2O_4$ on the NiO_xH_z and NiO surface in the process of the H_2 reduction. As a result, Ni particles were not fully reduced after the H_2 reduction, as described in Section 2.3. Metallic Ni particles were reduced on the top of the surface of the support, and the dehydrated NiO particles, which were not reduced, were on the sub-surface near the support [56], as shown in Figure 12a (II). As

compared with the NaOH_T catalyst, the fresh catalyst ($NaHCO_3$_T) using the $NaHCO_3$ titration method had fewer water molecules in the process of H_2 reduction because of the fine crystallite size (Figure 3) of NiO_xH_z ($Ni(OH)_2$) on the calcined LDH support, and the low content of the Ni element, as illustrated in Figure 7. Hence, the $NaHCO_3$_T catalyst can fully contribute to the reduction of the metallic Ni within an H_2 atmosphere, as shown in Figure 12b (II). Figure 12a (III) shows the formation of carbon on the surface of the NaOH_T + R catalyst during the ESR reaction at the initial work condition of the catalyst. The mixed nickel compounds (NiO) that favor the interaction with calcined LDH and are located in the sub-surface region near the support can form relatively large particles [56]. The schematic model displayed in Figure 12a (II) shows that the top of the layer is the Ni particles, and the second layer is the NiO particles. It is a possible that the aggregation of NiO particles blocked the path or reduced the number for the diffusion of carbons to the support. As as result, some of the carbons were formed in the sub-surface near the support, and the others were formed through the Ni particles in the layer of the surface of NiO particles, as shown in Figure 12a (III). Figure 12b (III) shows the carbon formation of the $NaHCO_3$_T + R catalyst at the initial work condition during the ESR reaction. The carbons can easily diffuse through the smaller Ni clusters in the ESR reaction [35,57–60]. After the diffusion of the carbons, they interact with the calcined LDH support. The previous study [61,62] indicated that methane C–H bonds can be cleaved at the Lewis acid sites in γ-Al_2O_3. Thereafter, hydrogen is desorbed by proton-hydride recombination, and carbon remains on the surface of the support. Finally, the carbons were accumulated in the interface region between Ni clusters and the calcined LDH support, as shown in Figure 12b (III). Figure 12a,b (IV) show the schematic models of catalysts (NaOH_T + R and $NaHCO_3$_T + R), respectively, in nano-scales at a longer period of the ESR reactions. Figure 12a (IV) presents the carbon deposition continuously and then the growths of filamentous carbon on the surface of the NaOH_T + R catalyst at a longer period of the ESR reactions. Previous studies [56,60] have indicated that NiO_xH_z (NiO) cluster particles are more stably bound on the γ-Al_2O_3 support. These cluster particles do not easily detach from the γ-Al_2O_3 support in the reaction process of the catalyst, owing to the low contact angle. Ultimately, the NiO and the mixed Ni cluster particles become buried by filamentous carbon, deactivating the catalyst. Figure 11a shows the SEM surface microstructure of the NaOH_T + R catalyst after the ESR reaction, and shows a few Ni particles on the tips of carbon filaments. The SEM image proves consistent with the model mechanism in Figure 12a. Figure 12b (IV) presents the carbons deposition and the growths of filamentous carbon on the surface of the $NaHCO_3$_T + R catalyst at a longer period of the ESR reactions. This is because Ni particles have an obtuse contact angle with the calcined LDH (γ-Al_2O_3) support and the binding energy between them is low [56,60]. The Ni particles can easily detach from the surface of the calcined LDH support. Hence, as the carbon filaments grow from the surface of the calcined LDH support, the Ni particles rose to the tips of the carbon filaments rather than being buried or encapsulated in the filaments. The model mechanism corresponds to the SEM image in Figure 11b, in which many of the Ni particles are on the tips of the carbon filaments. Cunha et al., [63] claimed that using the filamentous carbon as a support material with the Ni catalyst in steam and dry reforming of methane can increase the stability of the Ni particle, preventing surface migration and coalescence. In this study, the formation of filamentous carbons may act as a substitute, such as the LDH support that provided Ni particles on the surface and continued to activate with ethanol steam for generating H_2.

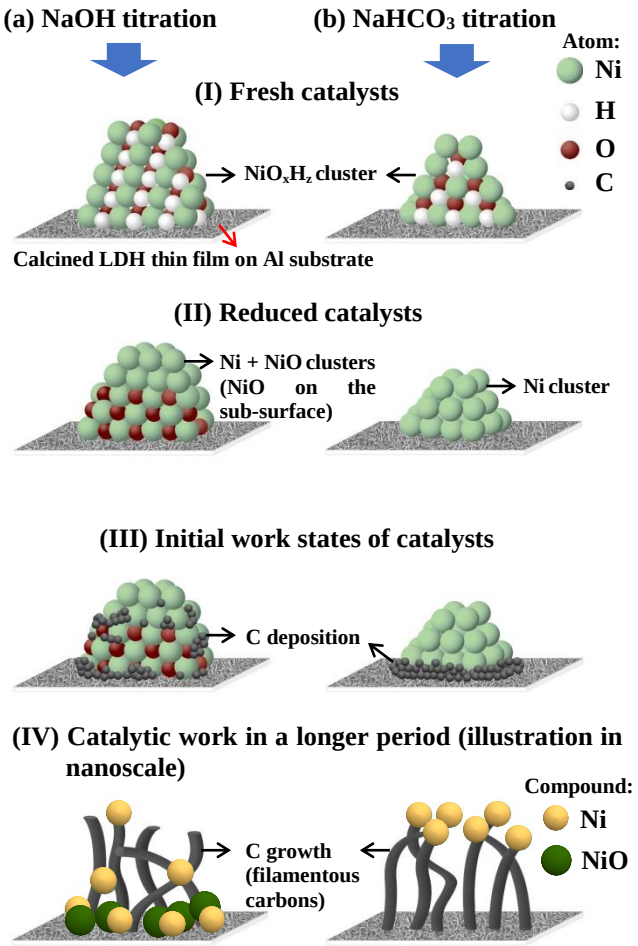

Figure 12. Schematic mechanisms illustrate the processes of carbon formation on the surfaces of the catalysts (Ni on calcined LDH) in the ESR reactions: (**a**) NaOH titrated catalysts and (**b**) $NaHCO_3$ titrated catalysts. The preparations of the catalysts and in the ESR reactions present in (I)–(IV): (I) Fresh catalysts; (II) Reduced catalysts; (III) Initial states of catalysts in the ESR reactions; (IV) NaOH titrated catalyst shows the formation of filamentous carbons burying gradually on the Ni and NiO particles; $NaHCO_3$ titrated catalyst shows that the Ni particles raise on the tips of the filamentous carbons. Note: The illustrations in (I)–(III) show processes in atomic scales, and (IV) shows in nanoscale.

Figure 13a depicts the temperature-programmed desorption (TPD) profiles of NH_3, which exhibits the information on the adsorption strength and density of acid sites on the surfaces of the NaOH_T + R and $NaHCO_3$_T + R catalysts. The adsorption peak in the low-temperature range from 50 to 200 °C is attributed to weak Lewis acid sites [64–66]. The weak acidity is reported in the previous study and indicates no or low catalytic activity [64]. The adsorption peaks in the intermediate to high temperature range (200–600 °C) are assigned to moderate to strong Lewis acid sites [64–66]. As shown in Figure 13a, the NaOH_T + R catalyst presented a broad desorption peak at about 200–600 °C, with the maximum intensity located at 338 °C. The $NaHCO_3$_T + R catalyst had three clear desorption peaks at about 298 °C, 386 °C, and 476 °C, respectively. The adsorption peak at 298 °C is probably attributed to the formation of $NiAl_2O_4$ species on the surface of the support (calcined LDH) [67,68]. The intensity of NH_3 adsorption at 298 °C on the NaOH_T + R catalyst was 1.5 times higher than with the $NaHCO_3$_T + R catalyst. Moreover, an asymmetric adsorption peak at about 430 °C on the NaOH_T + R catalyst may present the acid sites of NiO [69]. However, the $NaHCO_3$_T + R catalyst does not find any adsorption peak at 430 °C. It implies that more $NiAl_2O_4$, rather than reduced NiO, formed on the surface of the NaOH_T + R catalyst. The intensity of the NH_3-adsorption peak can be used to quantify the

acidity on the surface of the catalyst. Therefore, the areas of TPD curve in the intermediate to high-temperature range (200–600 °C) for the NaOH_T + R and $NaHCO_3$_T + R catalysts were, respectively, integrated. The sum of the integrated function of the NaOH_T + R catalyst had about 1.2 times higher than the $NaHCO_3$_T + R catalyst. In other words, the acidity of the NaOH_T + R catalyst was higher than the $NaHCO_3$_T + R catalyst. The result corresponds to the mechanism in Figure 12 and discussion in Section 2.3 that the $NiAl_2O_4$, and not reduced NiO on the NaOH_T + R catalyst, led to the increase of the density of the acid sites. In addition, Fang et al. [68] suggested that the highly dispersed Ni species can drop the acid sites because the nano Ni particles cover some acid sites on the surface of the catalyst. Hence, the $NaHCO_3$_T + R catalyst had low acidity when compared to the NaOH_T + R catalyst. Herein, the superior $NaHCO_3$_T + R catalyst was selected to perform the CO_2-TPD experiment to understand the characterization of the Li-Al mixed oxide supported catalyst on the acidic and basic properties. Figure 13b shows the CO_2-TPD profile of the $NaHCO_3$_T + R catalyst, which shows the adsorption strength and density of base sites on the surface of the catalyst. For comparing the acidic and basic properties of the $NaHCO_3$_T + R catalyst, the NH_3-TPD curve as shown in Figure 13a was replotted in Figure 13b. For the CO_2-TPD curve, the broad and weak adsorption peak in the low-temperature range from 100 to 200 °C is ascribed to low Brønsted basicity (i.e., surface OH- groups) [70–72]. There are two clear adsorption peaks around the intermediate to high-temperature range (200–600 °C), associated with moderate to strong Lewis basicity [70–72]. A peak at around 200–400 °C with the intermediate-strength Lewis basicity is attributed to the Li^+-O^{2-} and Al^{3+}-O^{2-} acid-base pairs [70–72]. Another strong peak at about 400–600 °C with strong Lewis basicity is related to the presence of low-coordinated O^{2-} [70–72]. The peak areas of the NH_3/CO_2-TPD can be determined as the amounts of acid and base sites of different strengths [73]. Hence, the amounts of acid and base sites in Figure 13b were calculated by integrating the sums of NH_3/CO_2 in each desorption peak. The resulting value of the ratio of acid/base sites was 0.519. A previous study [69] described that the base strength distribution of the M-Al mixed oxide relies on the M^{n+} metal cation (such as Li^+) used for incorporation with Al^{3+} cation (Li^+/Al^{3+}). In our study, the Li^+ promoter in the Al_2O_3 structure could effectively provide the Li^+-O^{2-} acid-base pairs. Particularly, the substitution of Al^{3+} by Li^+ in the Al_2O_3 lattice could substantially increase the O^{2-} on the surface of the catalyst [69]. It could also find that the CO_2-TPD curve (Figure 13b) had a strong adsorption peak located at 400–600 °C. The result suggested that the Li^+ promoter could effectively neutralize the acid sites in the Li-Al mixed oxide supported the $NaHCO_3$_T + R catalyst, reducing the dehydration of ethanol in the ESR process. The acidic property of the catalyst favors activating the ethanol, and leads to the dehydration of ethanol, as described by Equation (2). The C_2H_4 gas is the main product. Figure 13c presents the volumes of the C_2H_4 production for the $NaHCO_3$_T + R and NaOH_T + R catalysts during the ESR reactions, respectively. At the initial ESR reaction for 1 h, the $NaHCO_3$_T + R catalyst had only 1 L of C_2H_4 production. The NaOH_T + R catalyst showed four times more C_2H_4 production than the $NaHCO_3$_T + R catalyst. After the ESR reaction for 5 h, the $NaHCO_3$_T + R catalyst showed about half of the volume of C_2H_4 production, as compared with the NaOH_T + R catalyst. Moreover, ethanol can also dehydrate to $(C_2H_5)_2O$ [74,75], as described by Equation (11). The volumes of $(C_2H_5)_2O$ production using the $NaHCO_3$_T + R and NaOH_T + R catalysts during the ESR reactions are presented in Figure 13d. At the initial ESR reaction for 1 h, the $NaHCO_3$_T + R catalyst had small volumes of $(C_2H_5)_2O$ (0.17 L), while the NaOH_T + R catalyst had 0.89 L of $(C_2H_5)_2O$. The NaOH_T + R catalyst showed higher than five times the $(C_2H_5)_2O$ product when compared with the $NaHCO_3$_T + R catalyst. After the ESR reaction for 5 h, about 0.72 L of $(C_2H_5)_2O$ was produced by the $NaHCO_3$_T + R catalyst. The NaOH_T + R catalyst achieved nearly 2 L. The difference was about three times. The amounts of C_2H_4 and $(C_2H_5)_2O$ production were consistent with the NH_3-TPD curves, suggesting that the lower acidity on $NaHCO_3$_T + R catalyst had high H_2 selectivity and less dehydration of ethanol to produce C_2H_4 and $(C_2H_5)_2O$. Although the ethanol conversion of the NaOH_T + R

catalyst was higher than the $NaHCO_3$_T + R catalyst (Table 1), the high number of acid sites led to the activation of the dehydration of ethanol. As a result, the selectivity of the undesirable products, such as C_2H_4 and $(C_2H_5)_2O$, increased, while H_2 selectivity was reduced.

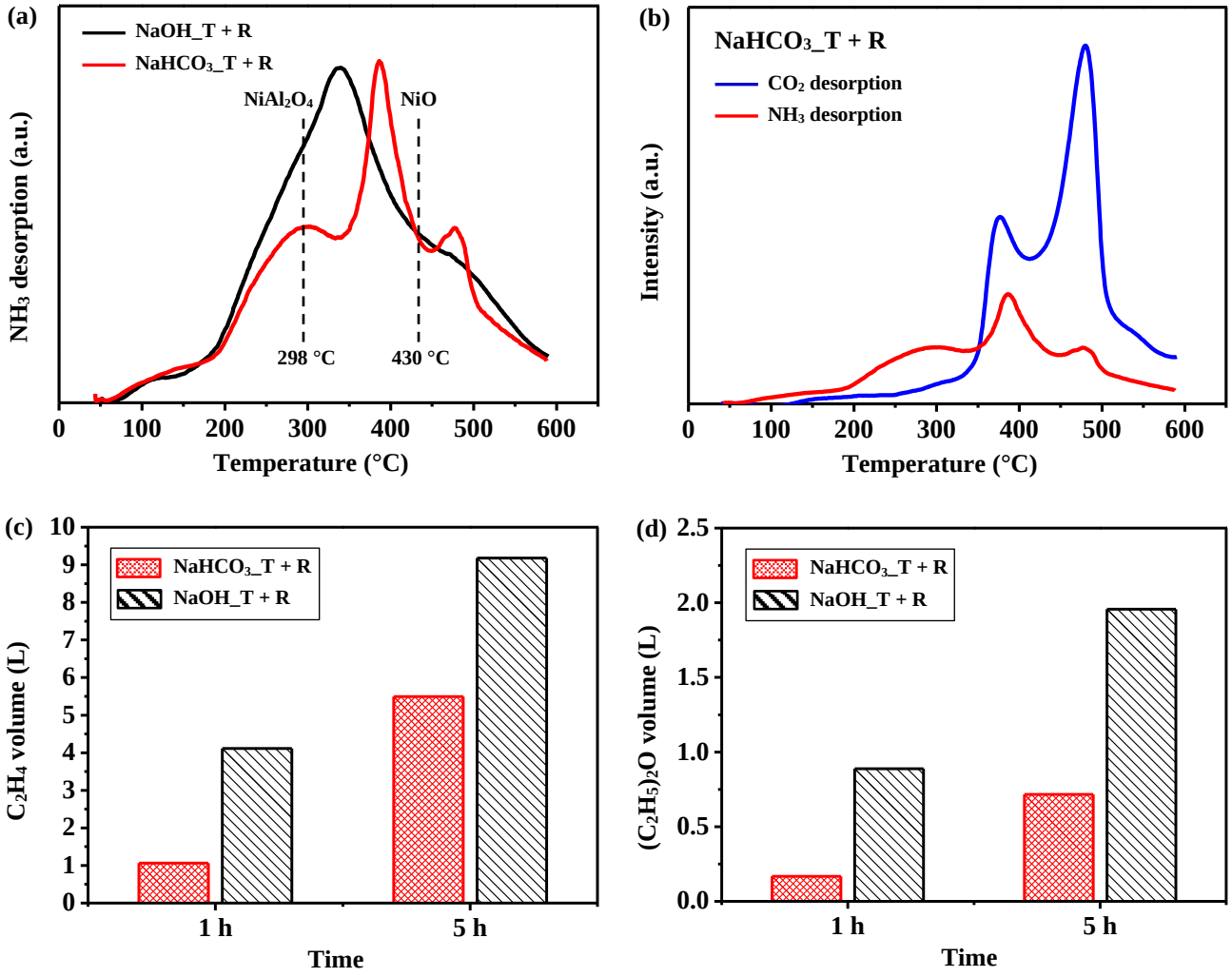

Figure 13. (**a**) NH_3-TPD profiles of the NaOH_T + R and $NaHCO_3$_T + R catalysts; (**b**) NH_3/CO_2-TPD profiles of the $NaHCO_3$_T + R catalyst; Gas volumes of the production of the NaOH_T + R and $NaHCO_3$_T + R catalysts at the initial and end states in the ESR reactions: (**c**) C_2H_4; (**d**) $(C_2H_5)_2O$.

3. Materials and Methods

3.1. Preparation and Calcination of Li-Al LDH Thin Film

The lathe strips from a 6061 aluminum alloy (Al-1 wt.% Mg–0.6 wt.% Si) rod were collected (C. S. Aluminium Co., Kaohsiung, Taiwan). The Al lathe waste strips were kneaded into a ball-like form with a diameter of approximately 50 mm. Before electrochemical deposition of the LDH, the ball-like Al lathe waste strip ball was ultrasonically cleaned in acetone and ethyl alcohol baths to remove debris and residual oil, and then were dried in air. Reagent-grade $LiOH{\cdot}H_2O$ was dissolved in deionized (DI) water at 50 °C, and highly pure Ar gas was purged through the LiOH aqueous solution (Choneye Pure Chemicals, Taipei, Taiwan). Small pieces of Al foil (~1 × 5 mm) were added to the stirred LiOH aqueous solution (0.06 M) at 50 °C for 30 min, and then the solution was filtered to obtain an electrolyte solution. The Li/Al molar ratio is 1:2. In the electrochemical deposition, the anode was a platinum-coated titanium mesh, and the cathode was the ball-like Al lathe waste strip ball. A DC voltage of 5V was applied between the platinum-coated titanium mesh and the Al lathe waste strip ball for 2 h using a Princeton Applied Research Model

273 A Potentiostat/Galvanostat. The preparation of the electrochemical experiment was described in detail in our earlier study [25]. After electrodeposition, the LDH-coated Al lathe waste strip ball was cleaned in DI water and dried in the ambient atmosphere. Subsequently, the Li-Al-CO_3 LDH thin films were calcined in air at various temperatures from 100 °C to 500 °C for 1 h in order to find the optimum condition to increase the hydrophilicity of the calcined LDH surface. Water contact angles were measured on the LDH and calcined LDH thin film surfaces.

3.2. Preparation of Ni-Based Catalyst on Calcined LDH Thin Film

Reagent-grade $NiCl_2$ (Shimakyu's Pure Chemicals, Osaka, Japan), NaOH, and $NaHCO_3$ (Choneye Pure Chemicals, Taipei, Taiwan) were used in the preparation of the catalysts. Ni catalysts were prepared using the following two methods: NaOH titration and $NaHCO_3$ titration. Al lathe waste strip balls that were coated with 400 °C calcined LDH thin films were immersed in 0.15 M $NiCl_2$ aqueous solutions at 50 °C. Then, the 1.25 M NaOH and 1.14 M $NaHCO_3$ aqueous solutions were, respectively, titrated into two cups of 0.15 M $NiCl_2$ aqueous solutions that both contained the Al lathe waste strip balls with the calcined LDHs. When the pH value of the 0.15 M $NiCl_2$ aqueous solutions dropped to 6.7, the titrations of the NaOH and $NaHCO_3$ solutions were stopped, and the Al lathe waste strip balls with the calcined LDHs were continuously immersed in the solutions for hours in order to form Ni precursors on the calcined LDH platelets' surfaces. The Al lathe waste strip ball sample that was processed by titrating the NaOH solution was denoted as NaOH_T. The Al lathe waste strip ball sample that was processed by titrating the $NaHCO_3$ solution was denoted as $NaHCO_3$_T. The samples of NaOH_T and $NaHCO_3$_T were then reduced in highly pure H_2 gas (3 L/min) in a furnace at 500 °C for 3 h, and then furnace-cooled to room temperature. Upon H_2 reduction, samples NaOH_T and $NaHCO_3$_T became NaOH_T + R and $NaHCO_3$_T + R, respectively. According to weight change measurements between an Al lathe waste strip ball that was coated with 400 °C calcined LDH thin film and the ball with a catalyst (NaOH_T + R or $NaHCO_3$_T + R), there was about 55 mg of Ni catalyst in one Al lathe strip framework.

3.3. Tests of Catalysts in Ethanol Stream Reforming (ESR)

For each test of the ESR experiment, six pieces of ball-like Al lathe frameworks with catalysts (NaOH_T + R or $NaHCO_3$_T + R) were packed together in a stainless steel tubular reactor for ESR (Chi Huw Heating Co., Ltd., Taiwan). The tubular reactor had a size of 60 mm in diameter and 450 mm in length. In the catalyzed ESR process, the catalysts were tested under atmospheric pressure. Water/ethanol mixture with a molar ratio of 7.5 was fed in, flowing at 10 mL/min, using a diaphragm pump (SIMDOS 02, KNF Neuberger, Switzerland) into the preheating chamber at 250 °C. Highly pure N_2 gas was used as the carrier gas. The mixed solution was vaporized in this preheating chamber at 250 °C, and then the mixed steam (ethanol and water) was inputted into the catalyst reactor at 500 °C. The ESR reaction began in the catalyst reactor at 500 °C. During the ESR reaction, the exhaust gases from the catalyst reactor were cooled and dried, and the liquid productions were condensed in a cold trap. The gaseous and liquid productions were analyzed using a VARIO PLUS enhanced flue gas analyzer (MRU-VARIO PLUS, Germany) and gas chromatography-mass spectrometry (GC-MS; Agilent 7890CB, USA, and JEOL AccuTOF-GCX, Japan).

3.4. Characterization

The crystal structures of Li-Al-CO_3 LDH thin film and fresh catalysts were examined using glancing angle X-ray diffraction (GAXRD; Bruker, Darmstadt, Germany), with an incidence angle of 0.5°, and a Bruker D8 Advance ECO diffractometer with Cu K_α (λ = 1.5406 Å) radiation at 40 kV and 25 mA. Fourier transform infrared (FT-IR) spectra of the fresh catalysts were obtained using a Perkin Elmer Spectrum 65 FT-IR spectrometer in the range 4000–400 cm^{-1}, at a resolution of 4 cm^{-1} (Perkin Elmer, Norwalk, CT,

USA). Surface microstructure images of the supports, catalysts, and catalysts after ESR were obtained by field-emission scanning electron microscopy (FE-SEM; JEOL JSM-6700F, Tokyo, Japan) in the secondary electron imaging mode, with an accelerating voltage of 3 kV and an emission current of 10 μA. Energy-dispersive X-ray spectra (EDS) were obtained using a JEOL JSM-6700F FE-SEM with an acceleration voltage of 15 kV to determine the elemental contents and their distributions of fresh catalysts and catalysts after the ESR reaction. The surface chemical compositions of reduced Ni catalysts were obtained by X-ray photoelectron spectroscopy (XPS; ULVAC-PHI 5000 VersaProbe/Scanning ESCA Microprobe, Kanagawa, Japan/USA) with monochromatic Al K_α radiation (1486.6 eV). The X-ray source operated at 15 kV (25 W). Before XPS analysis, a sputtering area of 2×2 mm^2 was firstly pre-cleaned by sputtering at 2 kV with Ar ions for 0.3 min to remove surface-adsorbed molecules and contamination. A focused ion beam (FIB; Hitachi NX2000, Tokyo, Japan) was used to prepare a specimen for cross-sectional transmission electron microscopic (TEM) observation. The cross-sectional microstructure images and diffraction pattern of the reduced catalysts were obtained with a field-emission transmission electron microscope (FE-TEM; FEI EO Tecnai F20 G2 MAT S-TWIN Field Emission Gun, Hillsboro, OR, USA) at an accelerating voltage of 200 kV. Temperature programmed desorption (TPD) profiles of NH_3 and CO_2 of the reduced catalysts were obtained using a Quantachrome Autosorb iQ TPX instrument (Anton Paar, Graz, Austria). The mixed NH_3/He or CO_2/He gases flowed through the sample for 0.5 h at a room temperature of 25 °C. Subsequently, a steady flow of He gas was passed through the sample for 0.5 h to remove the weakly adsorbed NH_3/CO_2 on the surface. Finally, the sample was heated from 25–600 °C with a heating rate of 10 °C/min in an He-flowing atmosphere.

4. Conclusions

Recycled aluminum lathe waste strips were able to be a framework, used in structured catalysts for the ethanol steam reforming reaction. Li-Al-CO_3 LDH (hydrotalcite) nanoplatelets were successfully electrodeposited on the surface of the Al lathe waste framework. The LDH nanoplatelets with an interplatelet space of about 400 nm could highly increase the specific surface area of the Al lathe waste strips. The LDH after calcination could raise the hydrophilicity of the surface, aiding the adsorption with the $NiCl_2$ aqueous solution in the preparation of the catalyst. The Ni precursors were easily prepared by in situ growth in the $NiCl_2$ aqueous solutions at 50 °C, with the NaOH and $NaHCO_3$ titration solutions used to adjust the pH at 6.7, respectively. The Ni precursor using the NaOH or $NaHCO_3$ titration method could form the same crystal of α-type nickel hydroxide ($Ni(OH)_2 \cdot xH_2O$). However, the amount of Ni precursor using the NaOH titration method was about two times higher than with the $NaHCO_3$ titration method. This is because the $Ni(OH)_2 \cdot xH_2O$ could dehydrate to NiO at 500 °C, simultaneously releasing the water vapor. The Ni precursor ($Ni(OH)_2 \cdot xH_2O$) on a calcined LDH (γ-Al_2O_3) support of the NaOH titrated sample may possess an excessive concentration of water vapor (in comparison to $NaHCO_3$_T) in the H_2 reduction process at 500 °C, inhibiting the reduction of $Ni(OH)_2 \cdot xH_2O$ to Ni particles. Hence, the Ni particles were not fully reduced in the H_2 reduction process. Nonstoichiometric $NiAl_2O_4$ that decorated the corners and edges of nickel crystallites retarded NiO reduction. NiO particles that were not reduced to Ni particles were likely formed in the sub-surface near the calcined LDH support. The result from the mechanism of carbon formation indicated that the mixed Ni cluster particles and NiO particles were buried by filamentous carbon during the ESR reaction. The Ni precursor of the $NaHCO_3$ titrated sample obtained a fill reduction of metallic Ni particles due to the small amount of water vapor in the H_2 reduction process. After the reduction in the H_2 atmosphere at 500 °C, Ni particles could uniformly disperse on the edges and platelets of the calcined LDH support. Because the Ni particles had an obtuse contact angle (low binding energy) with the calcined LDH support, the Ni particles could easily detach from the surface of the support to rise on the tips of the carbon filaments during the ESR reaction. The formation of filamentous carbons may act as a substitute, such as the LDH support

that provides Ni particles on the surface and continued to activate with ethanol steam in generating H_2. The mean Ni particle size on the $NaHCO_3$ titrated sample was 10.7 nm, which was smaller than the NaOH titrated sample (14.6 nm). Tests of catalytic activation of the $NaHCO_3$ titrated sample in the ESR for 5 h showed a stable H_2 yield of about 55 mol.%, and the rate of cumulative H_2 volume achieved was about 122.9 L/(g_{cat}·h). The main gas productions (H_2, CO_2, CO, and CH_4) had a stable output from the beginning to the end of the ESR reaction. The dehydration of ethanol showed a low selectivity to C_2H_4 (11.01%) and $(C_2H_5)_2O$ (2.57%), and deposition of carbon species of about 0.869 (g/(g_{cat}·h)), which was less than the NaOH titrated sample at 0.943 (g/(g_{cat}·h)). Possibly, Li^+ ions that existed in the mixed metal Li-Al-O oxide support neutralized the acid sites on the surface, decreasing Ni particle sintering. Conversely, the NiO particles with the $NiAl_2O_4$ wall on the surface of the NaOH titrated sample increased the number of acid sites. Although the ethanol conversion of the NaOH titrated sample (30.35%) was higher than the $NaHCO_3$ titrated sample (21.94%), the high number of acid sites led to the activation of the dehydration of ethanol. The selectivity of the C_2H_4 (20.93%) and $(C_2H_5)_2O$ (7.40%) were higher than the $NaHCO_3$ titrated sample. For the NaOH titrated sample, the H_2 yield decreased with time, and the rate of the cumulative H_2 volume was only about 87.2 L/(g_{cat}·h).

Supplementary Materials: The following supporting information can be downloaded at: https://www.mdpi.com/article/10.3390/catal12050520/s1, Figure S1: XRD pattern of the Li-Al LDH thin film on Al (A6061) substrate by electrochemical deposition. Figure S2: Water contact angle on the Al substrate, Li-Al LDH thin film @ Al substrate (L@Al), and Li-Al LDH thin film @ Al substrate (L@Al) after calcination at various temperatures. Figure S3: TEM bright-field images showed the distributions of Ni particles on the calcined LDH supports for the samples: (a) NaOH_T + R and (b) $NaHCO_3$_T + R.

Author Contributions: Conceptualization, J.-Y.U. and S.-H.H.; methodology, S.-H.H.; validation, J.-Y.U., S.-H.H., Y.-J.C. and W.-F.H.; formal analysis, S.-H.H.; investigation, S.-H.H.; resources, J.-Y.U.; data curation, S.-H.H.; writing—original draft preparation, S.-H.H.; writing—review and editing, S.-H.H.; visualization, J.-Y.U.; supervision, J.-Y.U.; project administration, S.-H.H.; funding acquisition, S.-H.H. All authors have read and agreed to the published version of the manuscript.

Funding: This study is financially supported by Ministry of Science and Technology, Taiwan (MOST 108-2221-E-005-034-MY3 and MOST 111-2923-E-194-002-MY3). The authors are grateful for their supports.

Data Availability Statement: The data that support the findings of this study are available on request from the corresponding author.

Conflicts of Interest: The authors declare no conflict to interest.

References

1. Benito, M.; Sanz, J.L.; Isabel, R.; Padilla, R.; Arjona, R.; Daza, L. Bio-ethanol steam reforming: Insights on the mechanism for hydrogen production. *J. Power Sources* **2005**, *151*, 11–17. [CrossRef]
2. Ni, M.; Leung, D.Y.C.; Leung, M.K.H. A review on reforming bio-ethanol for hydrogen production. *Int. J. Hydrogen Energy* **2007**, *32*, 3238–3247. [CrossRef]
3. Chang, W.-R.; Hwang, J.-J.; Wu, W. Environmental impact and sustainability study on biofuels for transportation applications. *Renew. Sustain. Energy Rev.* **2017**, *67*, 277–288. [CrossRef]
4. Lin, M.-Y.; Hourng, L.-W. Effects of magnetic field and pulse potential on hydrogen production via water electrolysis. *Int. J. Energy Res.* **2014**, *38*, 106–116. [CrossRef]
5. Wang, X.; Maeda, K.; Thomas, A.; Takanabe, K.; Xin, G.; Carlsson, J.M.; Domen, K.; Antonietti, M. A metal-free polymeric photocatalyst for hydrogen production from water under visible light. *Nat. Mater.* **2009**, *8*, 76–80. [CrossRef]
6. Sun, Y.; Jin, D.; Sun, Y.; Meng, X.; Gao, Y.; Dall'Agnese, Y.; Chen, G.; Wang, X.-F. G-C_3N_4/Ti_3C_2Tx (Mxenes) composite with oxidized surface groups for efficient photocatalytic hydrogen evolution. *J. Mater. Chem. A* **2018**, *6*, 9124–9131. [CrossRef]
7. Lin, M.-C.; Uan, J.-Y.; Tsai, T.-C. Fabrication of AlLi and Al_2Li_3/Al_4Li_9 intermetallic compounds by molten salt electrolysis and their application for hydrogen generation from water. *Int. J. Hydrogen Energy* **2012**, *37*, 13731–13736. [CrossRef]
8. Hosseini, S.E.; Abdul Wahid, M.; Jamil, M.M.; Azli, A.A.M.; Misbah, M.F. A review on biomass-based hydrogen production for renewable energy supply. *Int. J. Energy Res.* **2015**, *39*, 1597–1615. [CrossRef]
9. Abd El-Hafiz, D.R.; Ebiad, M.A.; Elsalamony, R.A.; Mohamed, L.S. Highly stable nano Ce–La catalyst for hydrogen production from bio-ethanol. *RSC Adv.* **2015**, *5*, 4292–4303. [CrossRef]

10. Chen, G.; Tao, J.; Liu, C.; Yan, B.; Li, W.; Li, X. Steam reforming of acetic acid using Ni/Al_2O_3 catalyst: Influence of crystalline phase of Al_2O_3 support. *Int. J. Hydrogen Energy* **2017**, *42*, 20729–20738. [CrossRef]
11. Olsson, L.; Hahn-Hagerdal, B. Fermentation of lignocellulosic hydrolysates for ethanol production. *Enzyme. Microb. Technol.* **1996**, *18*, 312–331. [CrossRef]
12. Huber, G.W.; Iborra, S.; Corma, A. Synthesis of transportation fuels from biomass: chemistry, catalysts, and engineering. *Chem. Rev.* **2006**, *106*, 4044–4098. [CrossRef] [PubMed]
13. Haryanto, A.; Fernando, S.; Murali, N.; Adhikari, S. Current status of hydrogen production techniques by steam reforming of ethanol: A review. *Energy Fuel* **2005**, *19*, 2098–2106. [CrossRef]
14. Phung, T.K.; Pham, T.L.M.; Nguyen, A.-N.T.; Vu, K.B.; Giang, H.N.; Nguyen, T.-A.; Huynh, T.C.; Pham, H.D. Effect of supports and promoters on the performance of Ni-based catalysts in ethanol steam reforming. *Chem. Eng. Technol.* **2020**, *43*, 672–688. [CrossRef]
15. Comas, J.; Mariño, F.; Laborde, M.; Amadeo, N. Bio-ethanol steam reforming on Ni/Al_2O_3 catalyst. *Chem. Eng. J.* **2004**, *98*, 61–68. [CrossRef]
16. Vaidya, P.D.; Rodrigues, A.E. Insight into steam reforming of ethanol to produce hydrogen for fuel cells. *Chem. Eng. J.* **2006**, *117*, 39–49. [CrossRef]
17. Mattos, L.V.; Jacobs, G.; Davis, B.H.; Noronha, F.B. Production of hydrogen from ethanol: Review of reaction mechanism and catalyst deactivation. *Chem. Rev.* **2012**, *112*, 4094–4123. [CrossRef]
18. Hou, T.; Zhang, S.; Chen, Y.; Wang, D.; Cai, W. Hydrogen production from ethanol reforming: Catalysts and reaction mechanism. *Renew. Sustain. Energy Rev.* **2015**, *44*, 132–148. [CrossRef]
19. Contreras, J.L.; Salmones, J.; Colín-Luna, J.A.; Nuño, L.; Quintana, B.; Córdova, I.; Zeifert, B.; Tapia, C.; Fuentes, G.A. Catalysts for H_2 production using the ethanol steam reforming (a review). *Int. J. Hydrogen Energy* **2014**, *39*, 18835–18853. [CrossRef]
20. Zanchet, D.; Santos, J.B.O.; Damyanova, S.; Gallo, J.M.R.; Bueno, J.M.C. Toward understanding metal-catalyzed ethanol reforming. *ACS Catal.* **2015**, *5*, 3841–3863. [CrossRef]
21. Sanchez-Sanchez, M.C.; Navarro, R.M.; Fierro, J.L.G. Ethanol steam reforming over Ni/M_xO_y-Al_2O_3 (M=Ce, La, Zr and Mg) catalysts: Influence of support on the hydrogen production. *Int. J. Hydrogen Energy* **2007**, *32*, 1462–1471. [CrossRef]
22. Elias, K.F.M.; Lucrédio, A.F.; Assaf, E.M. Effect of CaO addition on acid properties of Ni–Ca/Al_2O_3 catalysts applied to ethanol steam reforming. *Int. J. Hydrogen Energy* **2013**, *38*, 4407–4417. [CrossRef]
23. Huang, L.; Wang, J.; Gao, Y.; Qiao, Y.; Zheng, Q.; Guo, Z.; Zhao, Y.; O'Hare, D.; Wang, Q. Synthesis of $LiAl_2$-layered double hydroxides for CO_2 capture over a wide temperature range. *J. Mater. Chem. A* **2014**, *2*, 18454–18462. [CrossRef]
24. Sikander, U.; Sufian, S.; Salam, M.A. A review of hydrotalcite based catalysts for hydrogen production systems. *Int. J. Hydrogen Energy* **2017**, *42*, 19851–19868. [CrossRef]
25. Huang, S.-H.; Liu, S.-J.; Uan, J.-Y. Controllable luminescence of a Li–Al layered double hydroxide used as a sensor for reversible sensing of carbonate. *J. Mater. Chem.C* **2019**, *7*, 11191–11206. [CrossRef]
26. Tichit, D.; Gérardin, C.; Durand, R.; Coq, B. Layered double hydroxides: Precursors for multifunctional catalysts. *Top. Catal.* **2006**, *39*, 89–96. [CrossRef]
27. Feng, J.-T.; Lin, Y.-J.; Evans, D.G.; Duan, X.; Li, D.-Q. Enhanced metal dispersion and hydrodechlorination properties of a Ni/Al_2O_3 catalyst derived from layered double hydroxides. *J. Catal.* **2009**, *266*, 351–358. [CrossRef]
28. Li, M.; Wang, X.; Li, S.; Wang, S.; Ma, X. Hydrogen production from ethanol steam reforming over nickel based catalyst derived from Ni/Mg/Al hydrotalcite-like compounds. *Int. J. Hydrogen Energy* **2010**, *35*, 6699–6708. [CrossRef]
29. Vizcaíno, A.J.; Lindo, M.; Carrero, A.; Calles, J.A. Hydrogen production by steam reforming of ethanol using Ni catalysts based on ternary mixed oxides prepared by coprecipitation. *Int. J. Hydrog. Energy* **2012**, *37*, 1985–1992. [CrossRef]
30. Serna, C.J.; Rendon, J.L.; Iglesias, J.E. Crystal-chemical study of layered $[Al_2Li(OH)_6]$+ x-· nH_2O. *Clays. Clay Miner.* **1982**, *30*, 180–184. [CrossRef]
31. Cavani, F.; Trifiro', F.; Vaccari, A. Hydrotalcite-type anionic clays: Preparation, properties and applications. *Catal. Today* **1991**, *11*, 173–301. [CrossRef]
32. Evans, D.G.; Slade, R.C.T. Structural aspects of layered double hydroxides. *Struct. Bond.* **2006**, *119*, 1–87.
33. Hernandez, M.J.; Ulibarri, M.A.; Cornejo, J.; Pena, M.J.; Serna, C.J. Thermal stability of aluminium hydroxycarbonates with monovalent cations. *Thermochim. Acta* **1985**, *94*, 257–266. [CrossRef]
34. Shumaker, J.L.; Crofcheck, C.; Tackett, S.A.; Santillan-Jimenez, E.; Crocker, M. Biodiesel production from soybean oil using calcined Li–Al layered double hydroxide catalysts. *Catal. Lett.* **2007**, *115*, 56–61. [CrossRef]
35. Bartholomew, C.H. Mechanisms of catalyst deactivation. *Appl. Catal. A Gen.* **2001**, *212*, 17–60. [CrossRef]
36. López, E.; Divins, N.J.; Anzola, A.; Schbib, S.; Borio, D.; Llorca, J. Ethanol steam reforming for hydrogen generation over structured catalysts. *Int. J. Hydrogen Energy* **2013**, *38*, 4418–4428. [CrossRef]
37. Cybulski, A.; Moulijn, J.A. *Structured Catalysts and Reactors*; CRC Press: Boca Raton, FL, USA, 2005.
38. Palma, V.; Ruocco, C.; Castaldo, F.; Ricca, A.; Boettge, D. Ethanol steam reforming over bimetallic coated ceramic foams: Effect of reactor configuration and catalytic support. *Int. J. Hydrogen Energy* **2015**, *40*, 12650–12662. [CrossRef]
39. Santander, J.A.; Tonetto, G.M.; Pedernera, M.N.; López, E. Ni/CeO2–MgO catalysts supported on stainless steel plates for ethanol steam reforming. *Int. J. Hydrogen Energy* **2017**, *42*, 9482–9492. [CrossRef]

40. Kapteijn, F.; Moulijn, J.A. Structured catalysts and reactors—Perspectives for demanding applications. *Catal. Today* **2020**, *383*, 5–14. [CrossRef]
41. Frusteri, F.; Freni, S.; Chiodo, V.; Spadaro, L.; Di Blasi, O.; Bonura, G.; Cavallaro, S. Steam reforming of bio-ethanol on alkali-doped Ni/MgO catalysts: Hydrogen production for mc fuel cell. *Appl. Catal. A Gen.* **2004**, *270*, 1–7. [CrossRef]
42. Oliva, P.; Leonardi, J.; Laurent, J.F.; Delmas, C.; Braconnier, J.J.; Figlarz, M.; Fievet, F.; de Guibert, A. Review of the structure and the electrochemistry of nickel hydroxides and oxy-hydroxides. *J. Power Sources* **1982**, *8*, 229–255. [CrossRef]
43. Kamath, P.V.; Subbanna, G.N. Electroless nickel hydroxide: Synthesis and characterization. *J. Appl. Electrochem.* **1992**, *22*, 478–482. [CrossRef]
44. Liu, X.-M.; Zhang, X.-G.; Fu, S.-Y. Preparation of urchinlike NiO nanostructures and their electrochemical capacitive behaviors. *Mater. Res. Bull.* **2006**, *41*, 620–627. [CrossRef]
45. Duan, G.; Cai, W.; Luo, Y.; Sun, F. A hierarchically structured $Ni(OH)_2$ monolayer hollow-sphere array and its tunable optical properties over a large region. *Adv. Func. Mater.* **2007**, *17*, 644–650. [CrossRef]
46. Li, J.; Yan, R.; Xiao, B.; Liang, D.T.; Lee, D.H. Preparation of nano-NiO particles and evaluation of their catalytic activity in pyrolyzing biomass components. *Energ. Fuel.* **2008**, *22*, 16–23. [CrossRef]
47. Zhu, Z.; Wei, N.; Liu, H.; He, Z. Microwave-assisted hydrothermal synthesis of $Ni(OH)_2$ architectures and their in situ thermal convention to NiO. *Adv. Powder Technol.* **2011**, *22*, 422–426. [CrossRef]
48. Song, Q.S.; Li, Y.Y.; Chan, S.L.I. Physical and electrochemical characteristics of nanostructured nickel hydroxide powder. *J. Appl. Electrochem.* **2005**, *35*, 157–162. [CrossRef]
49. Shangguan, E.; Chang, Z.; Tang, H.; Yuan, X.-Z.; Wang, H. Synthesis and characterization of high-density non-spherical $Ni(OH)_2$ cathode material for Ni–MH batteries. *Int. J. Hydrogen Energy* **2010**, *35*, 9716–9724. [CrossRef]
50. Zieliński, J. The effect of water on the reduction of nickel/alumina catalysts. *Catal. Lett.* **1992**, *12*, 389–394. [CrossRef]
51. Zieliński, J. Effect of alumina on the reduction of surface nickel oxide; morphology of the surfaces of the surfaces of Ni/Al_2O_3 catalysts. *J. Mol. Catal.* **1993**, *83*, 197–206. [CrossRef]
52. Zieliński, J. Effect of water on the reduction of nickel-alumina catalysts catalyst characterization by temperature-programmed reduction. *J. Chem. Soc. Faraday Trans.* **1997**, *93*, 3577–3580. [CrossRef]
53. Shalvoy, R.B.; Davis, B.H.; Reucroft, P.J. Studies of the metal–support interaction in coprecipitated nickel on alumina methanation catalysts using x-ray photoelectron spectroscopy (xps). *Surf. Interface Anal.* **1980**, *2*, 11–16. [CrossRef]
54. Jr, L.S.; Makovsky, L.E.; Stencel, J.M.; Brown, F.R.; Hercules, D.M. Surface spectroscopic study of tungsten-alumina catalysts using x-ray photoelectron, ion scattering, and raman spectroscopies. *J. Phys. Chem.* **1981**, *85*, 3700–3707.
55. Meng, F.; Li, X.; Li, M.; Cui, X.; Li, Z. Catalytic performance of CO methanation over La-promoted Ni/Al_2O_3 catalyst in a slurry-bed reactor. *Chem. Eng. J.* **2017**, *313*, 1548–1555. [CrossRef]
56. Czekaj, I.; Loviat, F.; Raimondi, F.; Wambach, J.; Biollaz, S.; Wokaun, A. Characterization of surface processes at the Ni-based catalyst during the methanation of biomass-derived synthesis gas: X-ray photoelectron spectroscopy (XPS). *Appl. Catal. A Gen.* **2007**, *329*, 68–78. [CrossRef]
57. Baker, R.T.K. Catalytic growth of carbon filaments. *Carbon* **1989**, *27*, 315–323. [CrossRef]
58. Helveg, S.; Lo´ pez-Cartes, C.; Sehested, J.; Hansen, P.L.; Clausen, B.S.; Rostrup-Nielsen, J.R.; Abild-Pedersen, F.; Nørskov, J.K. Atomic-scale imaging of carbon nanofiber growth. *Nature* **2004**, *427*, 426–429. [CrossRef]
59. Jeong, N.; Lee, J. Growth of filamentous carbon by decomposition of ethanol on nickel foam: Influence of synthesis conditions and catalytic nanoparticles on growth yield and mechanism. *J. Catal.* **2008**, *260*, 217–226. [CrossRef]
60. Zhou, L.; Li, L.; Wei, N.; Li, J.; Takanabe, K.; Basset, J.-M. Effect of $NiAl_2O_4$ formation on Ni/Al_2O_3 stability during dry reforming of methane. *ChemCatChem* **2015**, *7*, 2508–2516. [CrossRef]
61. Barbier, J. Deactivation of reforming catalysts by coking-a review. *Appl. Catal.* **1986**, *23*, 225–243. [CrossRef]
62. Bitter, J.H.; Seshan, K.; Lercher, J.A. Deactivation and coke accumulation during CO_2/CH_4 reforming over pt catalysts. *J. Catal.* **1999**, *183*, 336–343. [CrossRef]
63. Cunha, A.F.; Morales-Torres, S.; Pastrana-Martínez, L.M.; Martins, A.A.; Mata, T.M.; Caetano, N.S.; Loureiro, J.M. Syngas production by bi-reforming methane on an Ni–K-promoted catalyst using hydrotalcites and filamentous carbon as a support material. *RSC Adv.* **2020**, *10*, 21158–21173. [CrossRef]
64. Berteau, P.; Delmon, B. Modified aluminas: Relationship between activity in 1-butanol dehydration and acidity measured by NH_3 TPD. *Catal. Today* **1989**, *5*, 121–137. [CrossRef]
65. Navarro, R.M.; Sanchez-Sanchez, M.C.; Fierro, J.L.G. Structure and activity of Pt-Ni catalysts supported on modified Al_2O_3 for ethanol steam reforming. *J. Nanosci. Nanotechnol.* **2015**, *15*, 6592–6603. [CrossRef]
66. Yergaziyeva, G.Y.; Dossumov, K.; Mambetova, M.M.; Strizhak, P.Y.; Kurokawa, H.; Baizhomartov, B. Effect of Ni, La, and Ce oxides on a Cu/Al_2O_3 catalyst with low copper loading for ethanol non-oxidative dehydrogenation. *Chem. Eng. Technol.* **2021**, *44*, 1890–1899. [CrossRef]
67. Zheng, S.; Liu, B.S.; Wang, W.S.; Wang, F.; Zhang, Z.F. Mesoporous and macroporous alumina-supported nickel adsorbents for adsorptive desulphurization of commercial diesel. *Adsorp. Sci. Technol.* **2015**, *33*, 337–353. [CrossRef]
68. Fang, X.; Zhang, R.; Wang, Y.; Yang, M.; Guo, Y.; Wang, M.; Zhang, J.; Xu, J.; Xu, X.; Wang, X. Plasma assisted preparation of highly active $NiAl_2O_4$ catalysts for propane steam reforming. *Int. J. Hydrogen Energy* **2021**, *46*, 24931–24941. [CrossRef]

69. Nivangune, N.; Kelkar, A. Selective synthesis of dimethyl carbonate via transesterification of propylene carbonate with methanol catalyzed by bifunctional Li-Al nano-composite. *ChemistrySelect* **2019**, *4*, 8574–8583. [CrossRef]
70. Di Cosimo, J.I.; Diez, V.K.; Xu, M.; Iglesia, E.; Apesteguia, C.R. Structure and surface and catalytic properties of Mg-Al basic oxides. *J. Catal.* **1998**, *178*, 499–510. [CrossRef]
71. Coleman, L.J.I.; Epling, W.; Hudgins, R.R.; Croiset, E. Ni/Mg–Al mixed oxide catalyst for the steam reforming of ethanol. *Appl. Catal. A Gen.* **2009**, *363*, 52–63. [CrossRef]
72. Pavel, O.D.; Tichit, D.; Marcu, I.-C. Acido-basic and catalytic properties of transition-metal containing Mg–Al hydrotalcites and their corresponding mixed oxides. *Appl. Clay Sci.* **2012**, *61*, 52–58. [CrossRef]
73. Antoniak-Jurak, K.; Kowalik, P.; Michalska, K.; Próchniak, W.; Bicki, R. Zn-Al mixed oxides decorated with potassium as catalysts for HT-WGS: Preparation and properties. *Catalysts* **2020**, *10*, 1094. [CrossRef]
74. Marino, F.J.; Cerrella, E.G.; Duhalde, S.; Jobbagy, M.; Laborde, M.A. Hydrogen from steam reforming of ethanol. Characterization and performance of copper-nickel supported catalysts. *Int. J. Hydrog. Energy* **1998**, *23*, 1095–1101. [CrossRef]
75. Marino, F.; Boveri, M.; Baronetti, G.; Laborde, M. Hydrogen production from steam reforming of bioethanol using Cu/Ni/K/γ-Al2O3 catalysts. Effect of Ni. *Int. J. Hydrogen Energy* **2001**, *26*, 665–668. [CrossRef]